August 2013

Heat Transfer Analysis of Two Pass Cooling Channel of Gas Turbine Blade with Analytical Wall Function Turbulence Approach

Hitoshi Arakawa
University of Wisconsin-Milwaukee

HEAT TRANSFER ANALYSIS
OF TWO PASS COOLING CHANNEL
OF GAS TURBINE BLADE
WITH ANALYTICAL WALL FUNCTION TURBULENCE APPROACH

by

Hitoshi Arakawa

A Thesis Submitted in

Partial Fulfillment of the

Requirements for the Degree of

Master of Science

in Engineering

at

The University of Wisconsin-Milwaukee

August 2013

ABSTRACT

**HEAT TRANSFER ANALYSIS
OF TWO PASS COOLING CHANNEL
OF GAS TURBINE BLADE
WITH ANALYTICAL WALL FUNCTION TURBULENCE APPROACH**

by

Hitoshi Arakawa

**The University of Wisconsin-Milwaukee, 2013
Under the Supervision of Dr. Ryo S Amano**

This paper reports experimental and computational studies of heat transfer through a square duct with a sharp 180 degree turn. The main purpose of this research was to study heat transfer predictions using the Analytical Wall-Function (AWF). To compare the predicting performance of the AWF, the standard Log-Law Based Wall-Function (LWF) and a Low-Reynolds-number (LRN) k-ε model were applied. Their results were also compared with experimental results for validation. In addition, three extended forms of the AWF were tested. The AWF showed better results than the conventional wall-function based on a logarithmic law especially in separation and reattachment regions and closer results to the LRN model's results. The extended forms of the AWF did not show significant differences from the results of the original form for the prediction of the whole region, although they showed to-some-extend changes in impinging and recirculation zones.

TABLE OF CONTENTS

LIST OF FIGURES

LIST OF TABLES

LIST OF NOMENCLATURE

Symbols: Description

a: discretization coefficients

A: area of an interface of a control volume

A_b: total surface area of the stainless foil

A_T, B_T, C_T: model constants in the AWF

A_U, B_U, C_U: model constants in the AWF

B, C: model constants in the LWF

c_P: specific heat ratio at constant pressure

c_ε, c_μ: model constants

d: $=A/a$

D_h: hydraulic diameter

F: radiation view factor

I: current value

k k_P: turbulence energy, turbulence energy at node P

ℓ: length of the stainless foil, turbulent length scale or distance from the turn (negative; inlet direction, positive; outlet direction)

ℓ_e: the equilibrium length scale

Nu: Nusselt number

Nu_0: theoretical Nusselt number

P: pressure

P_k: production term of turbulence energy

Pr, Pr_t: Prandtl number(=0.71), turbulent Prandtl number

$\dot{Q}$: actual amount of the heat supply

$\dot{Q}_s$: amount of power input from a power supply

q_w: wall heat flux

Q_{cd}, Q_R: conductive heat loss and thermal radiation

R: resistance

Re, $\mathrm{Re_t}$: Reynolds number and turbulent Reynolds number

s: estimated standard deviation

S: source term, strain ratio or the cross-sectional area

T, T_a, T_r, T_w: temperature, atmospheric temperature, reference temperature, wall temperature

u: estimated standard uncertainty

U, U^+, U_τ, U_b: mean velocity, =U/U_τ, friction velocity, bulk velocity

V: voltage value [V]

y^+, y^*: normalized distances $y\, c_\mu^{1/4}\sqrt{k_P}/\nu$ and $y\sqrt{k_P}/\nu$

YC: YAP correction term

y_d, y_v: model constants

Greeks

α: growth ratio of eddy viscosity in the wall adjacent cell for the AWF model

α_θ: $= \alpha \mathrm{Pr}/\mathrm{Pr_t}$

$\alpha_\lambda, \gamma_\lambda$: model constants

Γ_ϕ: diffusion coefficient

δ_{ij}: Kronecker's delta

ε: emissivity of the stainless foil, or dissipation ratio of turbulence energy

$\tilde{\varepsilon}$: $= \varepsilon - 2\nu\left(\frac{\partial\sqrt{k}}{\partial x_j}\right)^2$

$\theta, \theta^+, \theta_\tau$: mean temperature,$= \theta/\theta_\tau$ and $= (\theta_w - \theta)\rho c_p U_\tau / q_w$

κ, κ_t: model constants

λ: thermal conductivity of working fluid and $= \tau_w/\tau_v$

λ_a: thermal conductivity of acrylic plate.

μ, μ_t: molecular viscosity and eddy viscosity

ν, ν_t: kinematic viscosity and kinematic eddy viscosity

ρ, ρ_r: density and electrical resistivity

σ: Stefan-Boltzmann constant

$\sigma_k, \sigma_\varepsilon, c_{\varepsilon 1}, c_{\varepsilon 2}$: model constants in the k-ε model

τ_w, τ_v: wall shear stress, shear stress at y_v

ϕ: general variable

Abbreviations

ADI: Alternating Direction Implicit

AWF: Analytical Wall Function

EVM: Eddy Viscosity Model

FVM: Finite Volume Method

LRN: Low Reynolds Number model

LS: Launder Sharma model

LWF: standard Log-law based Wall Function

RANS: Reynolds Averaged Navier Storks

SIMPLE: Semi-Implicit Method for Pressure-Linked Equations

TDMA: Tri-Diagonal Matrix Algorism

TIT: Turbine Inlet Temperature

WF: Wall Function

CHAPTER 1: INTRODUCTION

1.1 Conventional Log-Law Based Wall-Functions:

It is important to investigate how to model near-wall regions for computations of turbulent heat transfer studies because physical quantities such as velocity drastically change in the region. Low-Reynolds-number (LRN) models (e.g., Launder-Sharma model [1]) are turbulence models which can express this near-wall phenomenon with high accuracy. They solve the boundary layer including the viscous sub-layer with damping functions. However, they also require very fine mesh to solve the near-wall region, resulting in extremely expensive computation cost. It is known that LRN + k-ε models can require more than ten times the computation cost of WF + k-ε models for three-dimensional calculations. Conventional WF models such as the standard log-low based wall-function (LWF) [2] are based on logarithmic laws. The WF models can use much coarser mesh in the region by skipping the viscous sub-layer and the buffer region with the log-laws. Consequently, industrial engineers still routinely use the conventional WF models. However, the laws are not a universal rule and are available only for fully developed flow in simple configurations such as flat plates. Therefore, complex geometry necessarily deteriorates the performance of the WF models. Tomas et al.[3] measured velocity profiles in the near-wall region with different pressure gradient as shown in *figure* 1.1. As can be seen, departure from the logarithmic line becomes larger as the pressure gradient becomes higher. It is also seen that adverse pressure gradients have more significant impacts on the velocity profiles than favorable gradients. The LWF, one of the most popular WF models, was proposed in 1974 by Launder and Spalding with the assumption of semi-logarithmic variations of the near-wall velocity and temperature.

After the proposal, Chieng and Launder [4] improved the LWF by allowing for a linear variation of both the shear stress and the turbulent kinetic energy across the wall adjacent cell. Other researchers also attempted to improve the LWF (e.g., Amano [5] and Ciofallo and Collins [6]). However, their attempts were based on the log-laws. Since the empirical log-law formulas are valid only for fully developed turbulent flows and do not consider pressure gradients, it was difficult to obtain reasonable results in complex flows with a high pressure gradient. To deal with this pressure gradient problem, Barenblatt et al. [7] and Kader [8] proposed WF models considering pressure gradients and showed that it is possible to improve the LWF by considering a pressure gradient effect.

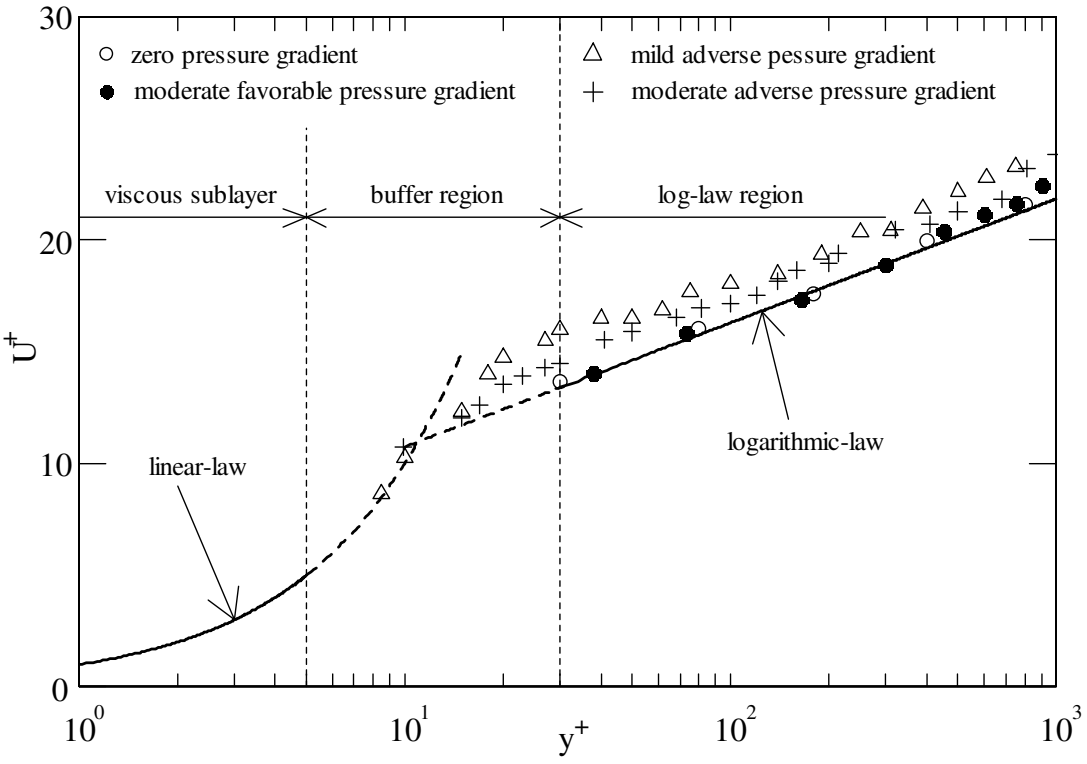

Figure 1.1: Mean velocity profiles in the near-wall region with different pressure gradients.

1.2 **The Analytical Wall-Functions:**

To ensure more reliable results from the WF models, several research groups have been developing new schemes during the last decade (e.g., Craft et al. [9], Knopp et al. [10], Popovac and Hanjalic´[11], and Utyuzhnikov [12]). A wall-function called analytical wall-function (AWF) [13] was proposed by Craft et al. The AWF has two main assumptions. One is the boundary layer theory; the AWF employs boundary layer approximated momentum and energy equations. The other is an eddy viscosity profile; in the AWF, the eddy viscosity is zero inside the viscous sub-layer and linearly increases above the layer. These assumptions make it possible to integrate the mean velocity and energy equations analytically over each wall adjacent cell. The AWF is based on the boundary layer theory, while the conventional WF models are empirical-laws-based models. Therefore, the AWF is expected to be more reliable in complex flows where the log-laws are not possible. Although the assumptions are still semi-empirical, they are less restrictive than the conventional WF models. It is consequently possible to introduce further refinements to the AWF to extend the range of flows that it can be applied to. Mostafa [14] proposed an extended AWF including a wall normal velocity component. A laminarization effect was proposed by Gerasimov [15]. Suga and Ishibashi [16] discussed a growth ratio of the eddy viscosity in the wall adjacent cells. In other cases, the AWF was extended to complex turbulent flows over rough, porous and gas–liquid surfaces (e.g., Suga [17], Suga and Nishiguchi [18] and Suga and Kubo [19]). Ultimately, the less restrictive assumptions make it possible to widen the range of the first layer thickness as well. The applicable range of the first layer thickness is $0<y^+<300$ for the AWF, $y^+<1$ for

LRN models and $30<y^{+}<300$ for the conventional WF models. Therefore, the AWF is expected to be a not only more reliable but also universal wall function.

1.3 **Gas turbines:**

The flow cases tested in this study was stationary two-pass channel with smooth wall. These flow cases mimic internal flows inside a gas turbine blade. The internal flows play a key role to improve gas turbine's efficiency. *Figure* 1.2 illustrates an outline of a gas turbine.

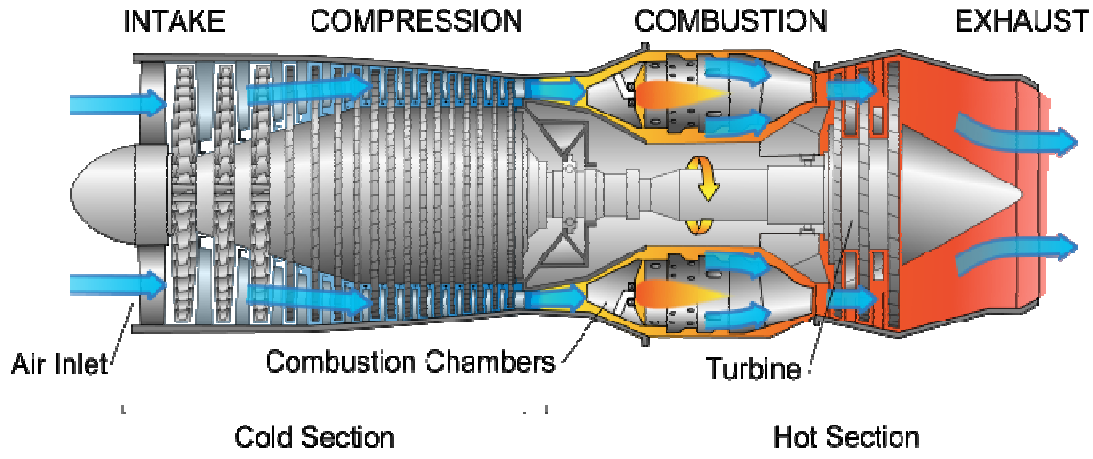

Figure 1.2: Gas turbine

Gas turbines are a kind of internal combustion engine obtaining power output by burning fuels such as light oil, kerosene and natural gas. A gas turbine takes in a great deal of air and compresses it in the compressor. The compressed air goes to the combustion room where the air gets mixed with the fuel. A high-temperature high-pressure flow is generated by igniting the mixture gas in the combustion room. This high-temperature high-pressure gas then enters the turbine part, where the gas expands and reduces the exhaust pressure, producing a shaft work output in the process. Gas turbines

are also used as thrusters, because they can produce impelling force by using the exhaust gas. They are consequently used everywhere, for example, power generators, aircrafts and trains. Therefore, the development of them is truly meaningful. To improve the performance, it is required to make the larger enthalpy difference between the inlet and the outlet. Since the pressure can be regarded as constant near the inlet, raising the inlet temperature is the same as raising the inlet enthalpy. Theoretically, it is possible to improve the performance by decreasing the outlet temperature. However, the outlet temperature is usually determined by the atmospheric temperature. For example, it is determined by the seawater temperature in a thermal power plant. Thus, this method is not reasonable from a practical standpoint. Consequently, gas turbines have a strong tendency to increase their turbine inlet temperature (TIT) as can be seen in *figure* 1.3 [20]. The first gas turbine was made in Sweden, and its output power was merely 400kw with 1000F TIT. The present TIT is over 1800F, and outstanding ones are over 2800F.

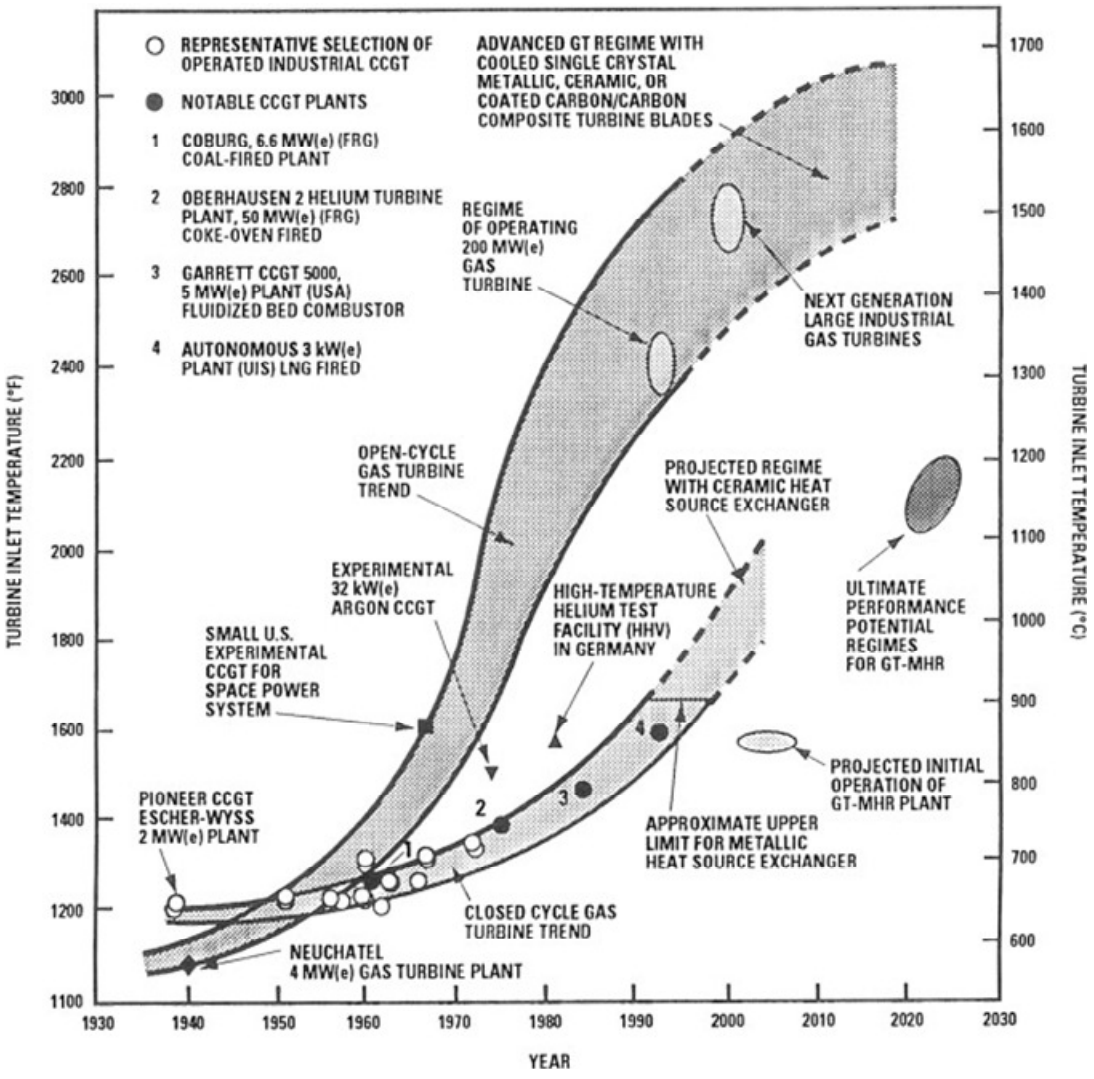

Figure 1.3: The recent trend of TIT.

1.3.1 **Cooling Problem:**

However, there are several difficulties to achieving high TIT. One of them is a cooling problem. Desired inlet temperatures exceed the melting temperature of the air foil material, which can be prevented if the turbine blades are effectively cooled. To improve the firing temperature and enhance the structural life of the blades, elaborate cooling systems seen in *figure* 1.4 [21] have evolved.

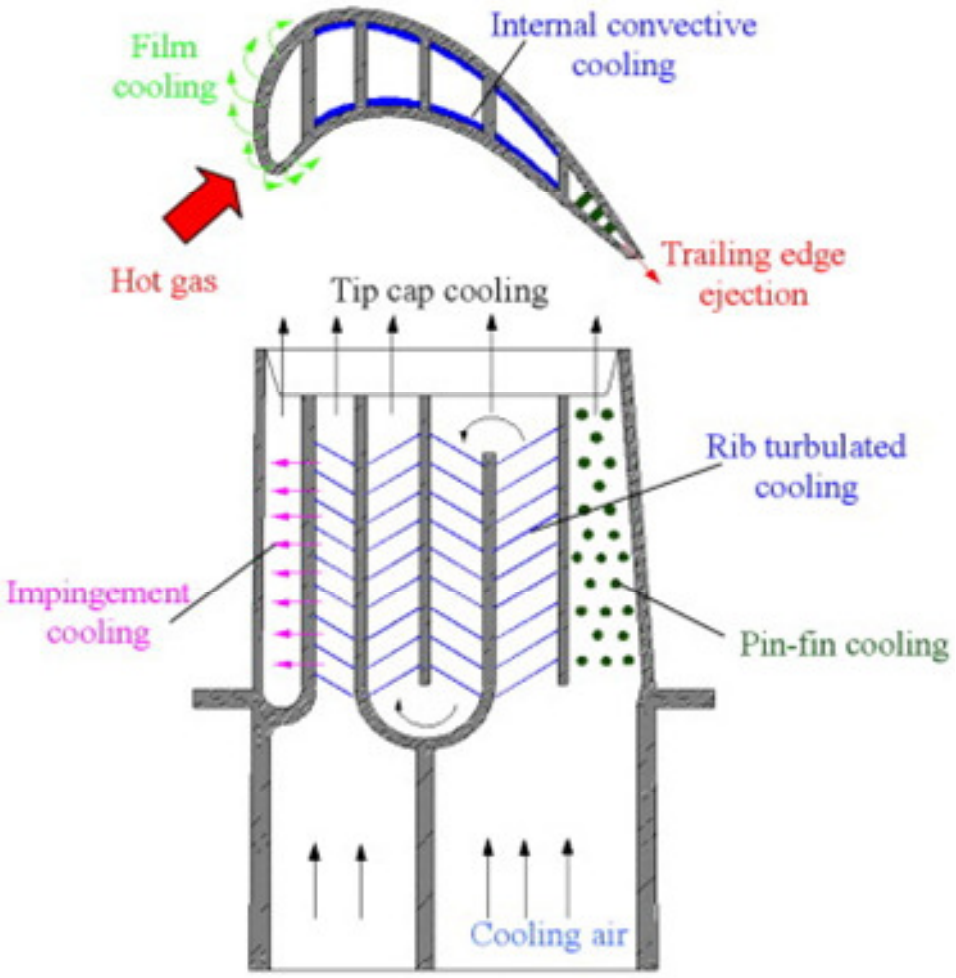

Figure 1.4: Cooling strategies and structure for gas turbine blades.

The flow inside such channels is complex and three dimensional, and becomes particularly complex as a result of sharp bends in the channels and rotation of the blades. An internal serpentine cooling passage inside the air foil was proven to yield a high heat transfer rate away from the blade surface, and is seen in more industrial utilization. To accomplish a high TIT, it is important to have a clear grasp of the cooling effects of gas turbine blades.

There have been many studies conducted, both experimental and computational, of the mass and heat transfer in a channel with a 180 degree turn. Sundén and Faghri [22], Goldstein [23] and Han [24] reported detailed measurements of local Nusselt numbers in non-rotating two-pass square channels. Iacovides et al. [25] also measured rotating effects in a two-pass channel. Since the advancement of computer resources has allowed us to use computation models requiring high resolution in grids such as LRN models, many studies using these models are also reported. (e.g., Su [26] and Iacovides et al. [27])

1.4 **Summarize:**

Several groups have researched the AWF and shown better results than the LWF, however, many of the studies were two-dimensional computations, and there are not many three-dimensional examples reported. Therefore, it is meaningful to examine the AWF's performance in such geometric conditions. Although the flow case tested in this study was relatively simple compared to the internal channels employed in real gas turbine blades because actual ones have ribs and rotate at high speed, it is three-dimensional and still has complex factors such as separations and reattachments. Thus, the flow case is good to investigate the basic performance of the AWF in three-dimensional computations. This study also employed a LRN k-ε model and the LWF model to evaluate the AWF's performance. Their results were also compared with the experimental results for validation.

CHAPTER 2: EXPERIMENTAL WORK

2.1 **Experimental Setup:**

*Figure*2.1 shows an outline of the experimental setup used in this study. The experiment used a two-pass square channel of 50.8mm side length (hydraulic diameter, D_h = 50.8mm). The set up was made of acrylic fiber. Air supplied from the blower goes through a honeycomb and then enters a digital readout meter where the flow velocity was measured via a Pitot tube (DWYER INSTRUMENTS©, DS-300). A stainless steel foil was used as a heating element. The metal foil was connected with a direct current stabilized power source supply (B&K PRECISION©, Model 1686A). The amount of heat supplied was adjusted by the power supply. Surface temperatures were measured using thirty thermocouples (OMEGA©, Type K) attached to the back of the stainless foil. Heat transfer characteristics on the heated surface were examined using Nusselt numbers calculated from the measured temperatures.

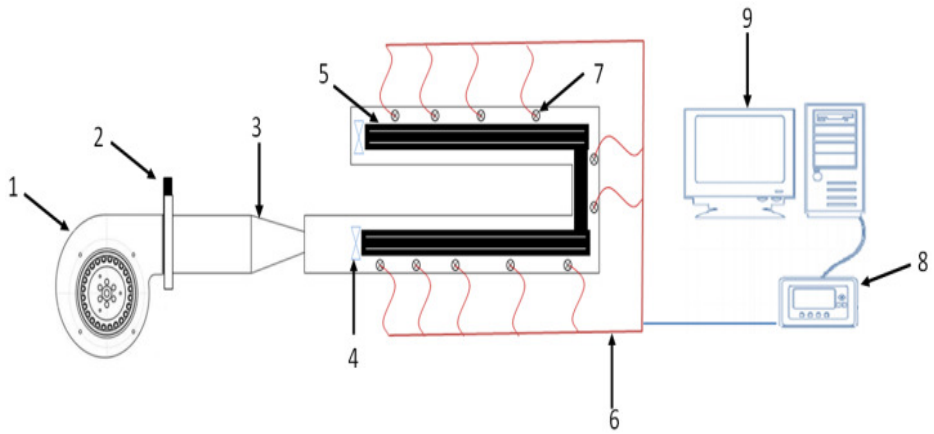

1.Blower
2.Damper
3.Reducer
4.Velocity Sensor
5.Heater
6.Thermocouples to DAQ Connection
7.Thermocouples
8.DAQ
9.Computer

Figure 2.1: Outline of the experimental setup.

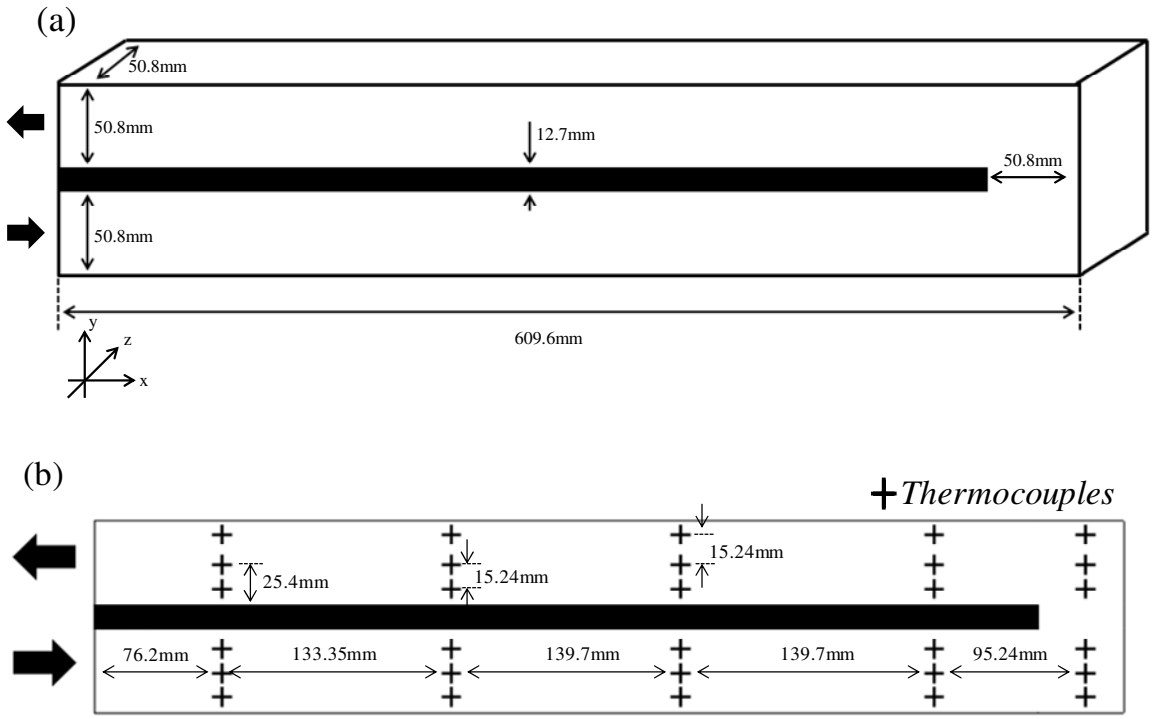

(a) Dimensions of the experimental setup

(b) Arrangement of measurement points

Figure 2.2: Details of the experimental setup.

2.2 **Measurement:**

2.2.1 **Velocity measurement:**

The inlet bulk velocity, U_b, was measured using a Pitot tube with a differential pressure transmitter (DWYER INSTRUMENTS©, MS-131-LCD) in this study. The Reynolds number was calculated using the following equation.

$$\mathrm{Re} = \frac{U_b D_h}{\nu}, \tag{2.1}$$

where v and D_h were the kinematic viscosity and the hydraulic diameter. The kinematic viscosity was assumed to be a constant of $1.51\times10^{-5}[m^2/s]$. The resultant Reynolds numbers were estimated to be 30,000, 60,000 and 90,000.

Table 2.1: Summary of the cases.

Working Fluid	Air		
Kinematic viscosity	$1.51\times10^{-5}m^2/s$		
Characteristic length scale	50.8mm		
Prandtl number	0.71		
Velocity	9.0m/s	18.0m/s	27.0m/s
Reynolds number	30,000	60,000	90,000

2.2.2 **Temperature measurement:**

The heat into the system is equal to the electrical power input. This study employed stainless foil as a heating element. The amount of power input, $\dot{Q}_s$, can be calculated from current, I, and voltage, V, in the foil.

$$\dot{Q}_s = I \cdot V. \tag{2.2}$$

However, the calculated $\dot{Q}_s$ from the above equation would be quite different from the actual heat gain since the resistance of the foil was smaller than the resistance of the other parts. Thus, this study used the following equation.

$$\dot{Q}_s = I^2 R, \tag{2.3}$$

where R is the resistance of the stainless foil. The resistance of the stainless foil was calculated by using the following relation:

$$R = \rho_R \frac{\ell}{S}, \tag{2.4}$$

where $\rho_R$is the electrical resistivity of the stainless foil(=72.0μΩm), ℓ is the length of the stainless foil and S is the cross-sectional area of the stainless foil.

2.3 **Heat loss estimation:**

A part of the heat supplied transfers to the acrylic plate and the atmosphere. The heat loss can be classified under conductive heat loss, $\dot{Q}_{cd}$, and thermal radiation, $\dot{Q}_R$.

$$\dot{Q} = \dot{Q}_S - \dot{Q}_{cd} - \dot{Q}_R. \tag{2.5}$$

$\dot{Q}_{cd}$ was estimated using the following equation.

$$\dot{Q}_{cd} = -\lambda_A A_b \frac{\partial T}{\partial z} = \lambda_A A_b \frac{T_1 - T_2}{z_{12}}. \tag{2.6}$$

Here, λ_A is the thermal conductivity of the acrylic plate ($\cong 0.21 \mathrm{W/m \cdot k}$) and A_b is the total surface area of the stainless foil. $T_1$and $T_2$are the temperatures of the stainless foil and the outer surface of the acrylic plate. $z_{12}$is the distance between $T_1$and T_2.

$\dot{Q}_R$ was estimated using the Stefan-Boltzmann law.

$$\dot{Q}_R = \varepsilon\sigma A(T_w^4 - T_a^4)F, \tag{2.7}$$

where, ε is the emissivity of the stainless foil ($\cong 0.11$), σ is the Stefan-Boltzmann constant ($\cong 5.6751 \times 10^{-8} \mathrm{W/m^2 \cdot k^4}$), $T_w$and T_a are the surface temperatures of the stainless foil and the atmospheric temperature, and F is the radiation view factor (=1). The resultant total heat loss was estimated to be around 3% and then summarized in *table* 2.2.

Table 2.2: Heat loss evaluation

Reynolds number	$\dot{Q}_{cd}$ %	$\dot{Q}_R$ %	Total %
30,000	2.96	2.24×10^{-3}	2.98
60,000	4.01	1.77×10^{-3}	4.02
90,000	3.08	1.15×10^{-3}	3.09
Average	3.35	1.72×10^{-3}	3.36

2.4**Nusselt number calculation:**

The actual heat supplied was then converted to the wall heat flux, q_w.

$$q_w = \dot{Q}/A_b. \tag{2.8}$$

The Nusselt number was calculated using the following equation.

$$\mathrm{Nu} = \frac{q_w D_h}{\lambda(T_w - T_r)}. \tag{2.9}$$

This study employed the fluid temperatures at middle height as the reference temperature, T_r. The theoretical Nusselt number was calculated from the Dittus-Boelter equation.

$$\mathrm{Nu}_0 = 0.0234 \times \mathrm{Re}^{0.8} \times \mathrm{Pr}^{0.4}, \tag{2.10}$$

where Pr is the Prandtl number for air (=0.71).

2.5 **Uncertainty evaluation:**

The uncertainty of the experiments was evaluated using a method called “Type A” in “A Beginner's Guide to Uncertainty of Measurement” [28]. The uncertainty can be calculated from the estimated standard uncertainty, *u*, of the mean:

$$u = \frac{s}{\sqrt{n}}, \tag{2.11}$$

where *s* and *n* are the estimated standard deviation and the number of the set. *s* can be expressed as:

$$s = \sqrt{\frac{\sum_{i=1}^{n}(x_i - \bar{x})^2}{n-1}}, \tag{2.12}$$

where x_i is the result of the *i* th measurement and $\bar{x}$ is the arithmetic mean of the *n* results considered. *Table* 2.3 shows the average uncertainty of the case. The total averaged error was estimated to be 4.80%, and the uncertainties of each point will be shown in chapter 4 as error bars.

Table 2.3: Uncertainty evaluation result.

Reynolds number	uncertainty, *u*/Nu%
30,000	5.10
60,000	5.18
90,000	4.11
Total	4.80

CHAPTER 3: CALCULATIONAL WORK

3.1 **Computational Procedure:**

This study employed a CFD code called the STREAM [29] developed by Manchester University in the UK. The STREAM code is a finite volume solver of three-dimensional incompressible Reynolds-Averaged Navier-Stokes (RANS) equations and an energy equation.

3.1.1 **Governing Equations:**

The STREAM code solves the equation of continuity, the Navier-Storks equations and the energy equation.

The continuity equation:

$$\frac{\partial U_i}{\partial x_i} = 0. \tag{3.1}$$

The Navier-Storks equations:

$$\rho \frac{DU_i}{Dt} = \frac{\partial}{\partial x_j}\left(\mu \frac{\partial U_i}{\partial x_j}\right) - \frac{\partial P}{\partial x_i}. \tag{3.2}$$

The energy equation:

$$\rho c_p \frac{D\Theta}{Dt} = \frac{\partial}{\partial x_j}\left(\lambda \frac{\partial \Theta}{\partial x_j}\right) + S_\Theta. \tag{3.3}$$

Here, the subscripts i and j denote the Cartesian coordinate system and follow the Einstein summation convention.

3.1.2 **Reynolds Averaging:**

The flow cases tested in the study were turbulent. Turbulent flows can be expressed as:

$$\phi(x,t) = \bar{\phi}(x) + \acute{\phi}(x,t). \tag{3.4}$$

Here, ϕ is a general variable, $\bar{\phi}$ is its time-averaged value and $\acute{\phi}$ is the fluctuating component. Considering that the time-averaged value of the fluctuating component is equal to zero, the resultant RANS equations become:

$$\rho\frac{\partial \bar{U}_\iota}{\partial t} + \rho\bar{U}_J\frac{\partial \bar{U}_\iota}{\partial x_j} = \frac{\partial}{\partial x_j}\left(\mu\frac{\partial \bar{U}_\iota}{\partial x_j}\right) - \frac{\partial \bar{P}}{\partial x_i} + \frac{\partial}{\partial x_j}\left(-\rho\overline{u_i' u_j'}\right). \tag{3.5}$$

Here, the last term of the right side of the equation is the Reynolds stresses. In the eddy viscosity model (EVM), the Reynolds stresses are approximated as:

$$-\rho\overline{u_i' u_j'} = \mu_t\left(\frac{\partial \bar{U}_J}{\partial x_i} + \frac{\partial \bar{U}_i}{\partial x_j}\right) - \frac{2}{3}\rho\delta_{ij}k, \tag{3.6}$$

where μ_t is the eddy viscosity, δ is the Kronecker's delta and k is the turbulence energy. This study used a linear k-ε model that solves k and ε equations to obtain the eddy viscosity (see section 3.2 for more details). The Reynolds-Averaged energy equation can be obtained in a similar manner,

$$\rho\frac{\partial \bar{\Theta}}{\partial t} + \bar{U}_J\frac{\partial \bar{\Theta}}{\partial x_j} = \lambda\frac{\partial^2 \bar{\Theta}}{\partial x_j^2} + \frac{\partial}{\partial x_j}\left(-\rho c_P\overline{u_j'\acute{\theta}}\right). \tag{3.7}$$

After this subsection, $\bar{\phi}$ is written as ϕ if there is no specific declaration.

3.1.3 **Discretization Method:**

The discretization method employed in the code is a finite-volume methodology (FVM) that embodies the conservation principle as an inherent property. The FVM integrates the governing equations over each small volume called control volume surrounding each node point on a mesh. A steady state transport equation for a general variable, ϕ, can be written as:

$$\frac{\partial}{\partial x_i}\left(\rho U_i - \Gamma_\phi \frac{\partial \phi}{\partial x_i}\right) = S_\phi, \tag{3.8}$$

where Γ_ϕ and S_ϕ are a diffusion coefficient and a source term, respectively. First, one-dimensionally methods will be described below. The FVM integrates *equation (3*.8) over a control volume highlighted in *figure* 3.1.

$$\left(\rho U\phi - \Gamma_\phi \frac{\partial \phi}{\partial x}\right)_e - \left(\rho U\phi - \Gamma_\phi \frac{\partial \phi}{\partial x}\right)_w = \overline{S_\phi} V, \tag{3.9}$$

where the subscripts *e* and *w* denote the east and west face illustrated in *figure* 3.1, and V denotes the control volume (V is Δx in one-dimensional problems, $\Delta x \Delta y$ for two-dimensional and $\Delta x \Delta y \Delta$z for three-dimensional).

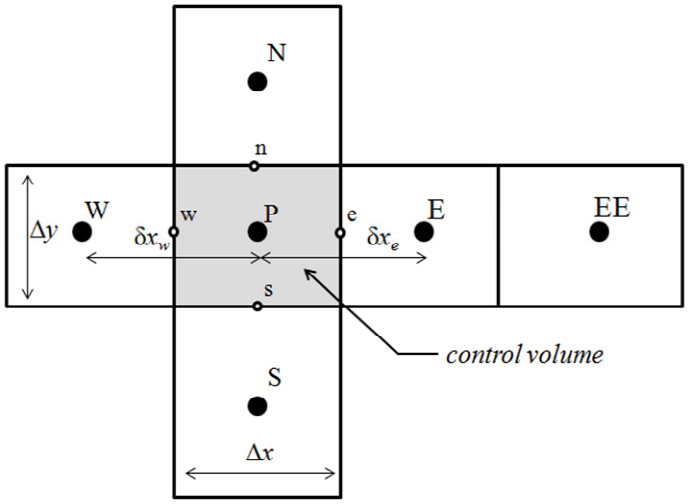

Figure 3.1: Two-dimensional arrangements of calculation points.

To obtain the unknown face values of the equation, some interpolations were used. The unknown face value, ϕ_f, can be obtained using an upstream nodal value, ϕ_U, a central nodal value, ϕ_C, and a downstream nodal value ϕ_D.

$$\phi_f = \phi_C + 0.5\varphi_{(r)}(\phi_C - \phi_U), \tag{3.10}$$

where $\varphi_{(r)}$ is a function of gradient ration *r* which is defined as below:

$$r = (\phi_D - \phi_C)/(\phi_C - \phi_U). \tag{3.11}$$

For the convection terms, the UMIST scheme [30] which is one of Cubic-Upstream-Interpolation schemes was employed.

$$\varphi_{(r)} = \tfrac{1}{4}\max\{0, \min(8r, 3r + 1, r + 3{,}8)\}. \tag{3.12}$$

For the diffusion terms, a Central-Differencing-Scheme (second order accurate) was used,

$$\varphi_{(r)} = r \tag{3.13}$$

The source term was discretized lineally as bellow:

$$\overline{S_\phi} = S_C + S_P\phi_P, \tag{3.14}$$

Insertion of these assumptions into *equation* (3.8) gives:

$$a_P\phi_P = \sum_{\text{nb=E,W}} a_{nb}\phi_{nb} + b, \tag{3.15}$$

where

$$a_E = \left(\frac{\Gamma_\phi}{\delta x}\right)_e A_e - \max\{(\rho U)_e, 0\}A_e, \tag{3.15a}$$

$$a_W = \left(\frac{\Gamma_\phi}{\delta x}\right)_w A_w - \max\{(\rho U)_w, 0\}A_w, \tag{3.15b}$$

$$a_P = \textstyle\sum_{nb=E,W} a_{nb} - S_P\,\mathrm{V}, \tag{3.15c}$$

$$b = S_C V, \tag{3.15d}$$

where, E and W denote the east and west faces, and A_f (here, A_f is $A_e$and A_w) denotes the area of the interface. (A_f is unity for one-dimensional problems and Δy for two-dimensional problems and ΔyΔz for three-dimensional.) By adding the other two directions to the *equation* (3.15), the three-dimensionally expanded discretized equation can be written as:

$$a_P\phi_P = \sum_{\text{nb=E,W,S,N,T,B}} a_{nb}\phi_{nb} + b, \tag{3.16}$$

where S,N,T and B denote the south, north, top and bottom direction, respectively.

3.1.4 **Pressure-Correction Method:**

To solve pressure fields, this study employed the SIMPLE [31] method handling velocity-pressure linkage. The originally proposed SIMPLE method used staggered mesh that pressure reference points are different from velocity reference points as shown in *figure* 3.2 to avoid checkerboard problems.

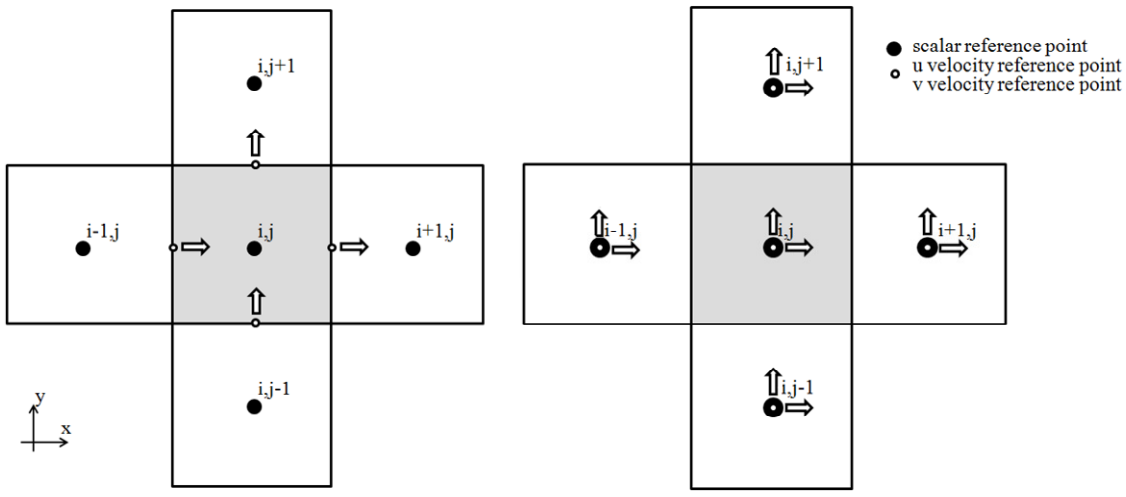

Figure 3.2: Staggered grids and co-located grids.

Since the staggered type requires more reference points than the co-located type as can be seen in the figure, this study employed the co-located type with an interpolation [32] proposed by Rhie and Chow. The original SIMPLE method calculates the pressure correction value $\acute{P}$ by substituting guessed pressure P^* and velocity U_i^* into the continuity equation, and then corrects the guessed pressure and velocity with the correction values. The guessed pressure can reach true value by repeating this procedure. The pressure correction equation and the velocity correction equation for *x* direction are:

$$P = P^* + \acute{P}, \tag{3.17}$$

$$U = U^* + \acute{U}. \tag{3.18}$$

The momentum equation for velocity *u* on the east face can be written from *equation* (3.16):

$$a_e U_e = \sum_{nb} a_{nb} U_{nb} + (P_P - P_E) A_e, \tag{3.19}$$

where, $A_e$is the area of the east surface. The guessed u^* velocity field can be obtained from:

$$a_e U_e^* = \sum_{nb} a_{nb} U_e^* + (P_P^* - P_E^*) A_e. \tag{3.20}$$

Since $\sum_{\mathrm{nb}} a_{nb} U_e'$ can be regarded to be zero, a velocity correction equation can be obtained from *equations* (3.19) and (3.20).

$$U_e' = d_e (P_P' - P_E'), \tag{3.21}$$

where $d_e = A_e / a_e$. The velocity corrections for the other directions can be obtained in the same way. The pressure correction can be obtained by substituting the velocity correction equations into the continuity equation. The one-dimensionally discretized form of the resultant equation is:

$$a_P p'_P = \sum_{nb=E,W} \mathrm{a_{nb}} p'_{nb} + b, \tag{3.22}$$

where

$$a_E = \rho_e d_e A_e, \tag{3.22a}$$

$$a_W = \rho_w d_w A_w, \tag{3.22b}$$

$$b = [(\rho u^*)_w - (\rho u^*)_e]\Delta y \Delta z, \tag{3.22c}$$

$$a_P = \sum_{nb=E,W} a_{nb}. \tag{3.22d}$$

The three-dimensionally pressure correction equation can be obtained by adding the other two directions.

$$a_P p'_P = \sum_{\mathrm{nb=E,W,N,S,T,B}} \mathrm{a_{nb}} p'_{nb} + S_C. \tag{3.23}$$

The Rhie-Chow interpolation separates the velocity into non-pressure part $\widehat{U}$and pressure part $d\Delta P$:

$$U = \widehat{U} - d\Delta P \tag{3.24}$$

Then, the velocity on the interface is interpolated with *equation* (3.24). For example, on an east face of a control volume,

$$U_e = \widehat{U}_e - d_e(P_E - P_P) \tag{3.25}$$

$$= (U + d\Delta P)_e - d_e(P_E - P_P)$$

$$= (U + d\Delta P)_e - d_e(P_E - P_P)$$

$$= \frac{1}{2}(U_E + U_P) + \frac{1}{2}(d_E\Delta P_E + d_P\Delta P_P) - d_e(P_E - P_P)$$

$$= \tfrac{1}{2}(U_E + U_P) + \tfrac{1}{2}\left\{\tfrac{1}{2}d_E(P_{EE} - P_P) + \frac{1}{2}d_E(P_E - P_W)\right\} - d_e(P_E - P_P)$$

Since U_e uses consecutive nodal pressure values, there is no zigzag pressure solution.

The STREAM code solves matrixes obtained from the discretized equations stated above, by using the TDMA (Tri-Diagonal Matrix Algorism) combined with ADI-type sweeps [33] (Alternating Direction Implicit or "line-by-line method"). This study adjusted the sweep directions in each block (this study employed multi-block method) for faster convergence.

3.2 **Turbulence Models:**

This study used a linear k-ε model (Launder-Sharma model [1] or LS model). The LS model is one of the LRN models. As stated below, the difference between the LRN models and WF models can be seen in the near-wall region. Thus, it is possible to use the WF models with the LS type k-ε model to solve the core region. That is, the LS type *k-ε* model solves the core region and a WF model solves the near-wall region, respectively.

3.2.1 **Modelling for Core Region:**

All models employed in the study use the LS type k-ε model to solve the core region. The transport equations of turbulence energy and its dissipation ratio can be written as:

$$\frac{Dk}{Dt} = \frac{\partial}{\partial x_i}\langle\left(\nu + \frac{\nu_t}{\sigma_k}\right)\frac{\partial k}{\partial x_i}\rangle + P_k - \varepsilon, \tag{3.26}$$

$$\frac{D\varepsilon}{Dt} = \frac{\partial}{\partial x_i}\langle\left(\nu + \frac{\nu_t}{\sigma_\varepsilon}\right)\frac{\partial \varepsilon}{\partial x_i}\rangle + C_{\varepsilon 1}\frac{\varepsilon P_k}{k} - C_{\varepsilon 2}\frac{\varepsilon^2}{k}, \tag{3.27}$$

and the kinematic eddy viscosity is calculated using *k* and *ε*.

$$\nu_t = c_\mu k^2/\varepsilon. \tag{3.28}$$

Table3.1: Model coefficients for the *k*-*ε* model.

σ_k	σ_ε	$c_{\varepsilon 1}$	$c_{\varepsilon 2}$	$\mathrm{c_\mu}$	$\mathrm{Pr_t}$
1.0	1.22	1.44	1.92	0.09	0.9

3.2.2 **Modelling for Near-Wall Region (the LS model):**

The LS model expresses the low-Reynolds-number effect using damping functions. The modified equations for near-wall region are,

$$\nu_t = C_\mu f_\mu \frac{k^2}{\tilde{\varepsilon}}, \tag{3.29}$$

$$\frac{D\tilde{\varepsilon}}{Dt} = \frac{\partial}{\partial x_i}\langle\left(\nu + \frac{\nu_t}{\sigma_\varepsilon}\right)\frac{\partial \tilde{\varepsilon}}{\partial x_i}\rangle + C_{\varepsilon 1} f_1 \frac{\tilde{\varepsilon} P_k}{k} - C_{\varepsilon 1} f_2 \frac{\tilde{\varepsilon}^2}{k} + 2\nu\nu_t\left(\frac{\partial^2 U_i}{\partial x_j \partial x_k}\right), \tag{3.30}$$

where $\tilde{\varepsilon} = \varepsilon - 2\nu\left(\frac{\partial\sqrt{k}}{\partial x_j}\right)^2$, $f_\mu = \exp\left(\frac{-3.4}{(1+R_t/50)^2}\right)$, $f_1 = 1.0$ and $f_2 = 1 - 0.3\exp\left(-{R_t}^2\right)$ with $R_t = k^2/(\nu\tilde{\varepsilon})$.

This study also employed a length-scale correction term called the Yap-correction [34] for the LS model. The correction term *YC* can be written as:

$$YC = 0.83\left(\frac{\tilde{\varepsilon}^2}{k}\right) max\left[\left(\frac{\ell}{\ell_e} - 1\right)\left(\frac{\ell}{\ell_e}\right)^2, 0\right] \tag{3.31}$$

here, ℓ is the turbulent length scale $k^{3/2}/\tilde{\varepsilon}$, ℓ_e is the equilibrium length-scale $c_\ell y$. This term was added to the ε equation as an extra source term.

3.2.3 **Modelling for Near-Wall Region (the LWF model):**

The LWF is one of the most popular conventional WF models used in practical applications, and is based on a logarithmic law. Mean velocity and temperature can be written as:

$$U^+ = \frac{1}{\kappa} lny^+ + B, \tag{3.32}$$

$$\Theta^+ = \frac{1}{\kappa_t} lny^+ + C, \tag{3.33}$$

where $U^+ = U/U_\tau$ and $\theta^+ = \theta/\theta_\tau$ with $U_\tau = \sqrt{\tau_w/\rho}$ and $\theta_\tau = (\theta_w - \theta)\rho c_p U_\tau/q_w$. y^+ is a dimensionless wall unit expressed as $y\, c_\mu^{1/4}\sqrt{k_P}/\nu$ (k_P is turbulence energy at node P). The values of κ, κ_t, B, and C are summarized in *table* 3.2

Table3.2: Model coefficients for the LWF

K	k_t	B	C
0.42	0.48	5.2	3.84

The wall shear stress and the heat flux can be easily obtained from the above equations.

$$\tau_w = \rho \left(\frac{U_P}{\frac{1}{\kappa} ln y_P^+ + B} \right)^2 \tag{3.34}$$

$$q_w = \frac{\rho c_P U_\tau (\theta_w - \theta_P)}{\frac{1}{k_t} ln\, y_P^+ + C} \tag{3.35}$$

Then, using an experimental result ($(-\overline{\acute{u}\acute{v}}/k)^2 = \mathrm{c_\mu} = 0.09$) and the definition of Reynolds stresses, the friction vector U_τ can be written as below:

$$U_\tau = \sqrt{\tau_w/\rho} = \sqrt{-\overline{\acute{u}\acute{v}}} = \sqrt{{c_\mu}^{1/2} k_P} = {c_\mu}^{1/4} {k_P}^{1/2} \tag{3.36}$$

The production term of turbulence energy at the node point in the wall adjacent cell, P_k is,

$$P_k = \nu_t \left(\frac{\partial U}{\partial y} \right)^2 = -\overline{\acute{u}\acute{v}} \left(\frac{\partial U}{\partial y} \right) = \frac{\tau_w}{\rho} \frac{U_\tau}{\kappa y} = \frac{{\tau_w}^2}{\rho \kappa {c_\mu}^{1/4} {k_P}^{1/2} y.} \tag{3.37}$$

Considering the effect of the viscous sub-layer, its cell-averaged value becomes:

$$\overline{P_k} = \frac{1}{y_n} \int_0^{y_n} P_k dy = \frac{1}{y_n} \int_{y_\nu}^{y_n} P_k \, dy = \frac{{\tau_w}^2}{\rho \kappa {c_\mu}^{1/4} {k_P}^{1/2} y_n} \ln[\frac{y_n}{y_\nu}]. \tag{3.38}$$

The dissipation ratio, ε ,is modeled as:

$$\varepsilon = \begin{cases} 2\nu\, k_P / y_\nu^2 & \text{for} \quad y < y_\nu \\ k_P^{1.5} / (c_\ell y) & \text{for} \quad y > y_\nu \end{cases} \tag{3.39}$$

Then, its cell-averaged value $\bar{\varepsilon}$ becomes:

$$\bar{\varepsilon} = \frac{k_P^{3/2}}{c_\ell y_n} \left(1 + \ln \left[\frac{y_n}{y_\nu} \right] \right). \tag{3.40}$$

3.2.4 **Modelling for Near-Wall Region (The Analytical Wall Function):**

The AWF has been developed as a more reliable WF model and is based on the boundary layer theory. The boundary layer approximated momentum and energy equations in the wall-adjacent cells are:

$$\frac{\partial}{\partial y^*}\left[(\mu+\mu_t)\frac{\partial U}{\partial y^*}\right]=\underbrace{\frac{\nu^2}{k_P}\left[\frac{\partial}{\partial x}(\rho UU)+\frac{\partial P}{\partial x}\right]}_{C_U} \tag{3.41}$$

$$\frac{\partial}{\partial y^*}\left[\left(\frac{\mu}{\mathrm{Pr}}+\frac{\mu_t}{\mathrm{Pr_t}}\right)\frac{\partial \theta}{\partial y^*}\right]=\underbrace{\frac{\nu^2}{k_P}\left[\frac{\partial}{\partial x}(\rho U\theta)-S_\theta\right]}_{C_T} \tag{3.42}$$

where $y^*=y\sqrt{k_P}/\nu$.The AWF assumes that the eddy viscosity μ_t is zero in the viscous sub-layer ($y^*<y_v^*$), and linearly increases above the layer ($y^*>y_v^*$) as shown in *figure* 3.3.

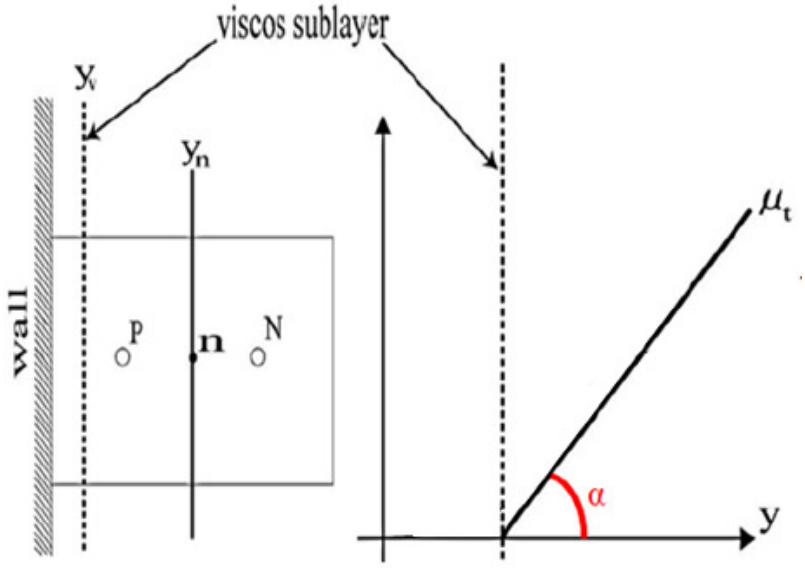

Figure 3.3: Near-wall treatment in the AWF.

$$\mu_t=\begin{cases}0 & \text{for } y^*<y_v^*\\ \alpha\mu(y^*-y_v^*) & \text{for } y^*>y_v^*\end{cases} \tag{3.43}$$

where $\alpha = c_\ell c_\mu = 2.55 \times 0.09$ and $y_v^* = 10.9$. Note that *x* and *y* directions denote the wall parallel direction and the wall normal direction respectively. Using these above assumptions, the mean velocity and temperature can be integrated over the wall-adjacent cell. The mean velocity and its gradient are

For $y^* < y_v^*$ (in the viscous sub-layer):

$$\frac{dU}{dy^*} = \frac{C_U y^* + A_U}{\mu}, \tag{3.44}$$

$$U = \frac{C_U}{2\mu} y^{*2} + \frac{A_U}{\mu} y^* + B_U. \tag{3.45}$$

For $y^* > y_v^*$ (above the viscous sub-layer):

$$\frac{dU}{dy^*} = \frac{C_U y^* + A_U}{\mu\{1 + \alpha(y^* - y_v^*)\}}, \tag{3.46}$$

$$U = \frac{C_U}{\alpha\mu} y^* + \left\{\frac{\acute{A}_U}{\alpha\mu} - \frac{C_U}{\alpha^2\mu}(1 - \alpha y_v^*)\right\} \ln[1 + \alpha(y^* - y_v^*)] + \acute{B}_U. \tag{3.47}$$

The mean temperature and its gradient are

For $y^* < y_v^*$ (in the viscous sub-layer):

$$\frac{d\theta}{dy^*} = \frac{\Pr\,(C_T y^* + A_T)}{\mu}, \tag{3.48}$$

$$\theta = \frac{\Pr C_T}{2\mu} y^{*2} + \frac{PrA_T}{\mu} y^* + B_T. \tag{3.49}$$

For $y^* > y_v^*$ (above the viscous sub-layer):

$$\frac{d\theta}{dy^*} = \frac{\Pr\,(C_T y^* + A_T)}{\mu\{1 + \alpha_\theta(y^* - y_v^*)\}}, \tag{3.50}$$

$$\theta = \frac{PrC_T}{\alpha_\theta\mu} y^* + \left\{\frac{Pr\acute{A}_T}{\alpha_\theta\mu} - \frac{PrC_T}{\alpha_\theta^2\mu}(1 - \alpha_\theta y_v^*)\right\} \times \ln[1 + \alpha_\theta(y^* - y_v^*)] + \acute{B}_T. \tag{3.51}$$

Here $\alpha_\theta = \alpha\,\mathrm{Pr}/\mathrm{Pr_t}$. Note that the integration constants can be obtained from the boundary conditions at $y^* = 0, y^* = y_v^*$ and $y^* = y_n^*$.

$$\begin{cases} U = 0 & \text{at } y = 0 \\ U = U_n & \text{at } y = y_n \\ U \text{ and } \partial U/\partial y \text{ are continus} & \text{at } y = y_v \end{cases} \tag{3.52}$$

The wall shear stress and the wall heat flux that can be obtained from resultant mean velocity and temperature gradients.

$$\tau_w = \mu \frac{\partial U}{\partial y}\Big|_w = \mu \frac{k_p^{1/2}}{\nu}\frac{\partial U}{\partial y^*}\Big|_w = \frac{k_p^{1/2} A_U}{\nu}, \tag{3.53}$$

$$\begin{aligned} q_w &= -\frac{\rho c_P \nu}{\mathrm{Pr}}\frac{\partial \theta}{\partial y}\Big|_w \\ &= -\frac{\rho c_P \nu}{\mathrm{Pr}}\frac{k_p^{1/2}}{\nu}\frac{\partial \theta}{\partial y^*}\Big|_w = \frac{\rho c_P k_p^{1/2} A_T}{\nu}. \end{aligned} \tag{3.54}$$

The production of turbulence energy$P_k (= \nu_t (\partial U/\partial y)^2)$ can be written as:

$$P_k = \begin{cases} 0 & \text{for } y^* > y_v^* \\ \dfrac{\alpha k_p}{\nu}(y^* - y_v^*)\left\{\dfrac{C_U y^* + \acute{A}_U}{\mu(1 + \alpha\{y^* - y_v^*\})}\right\}^2 & \text{for } y^* \le y_v^* \end{cases} \tag{3.55}$$

Then, its cell-averaged value$\overline{P_k}$ used to solve the k equation is obtained by integrating it over the wall-adjacent cell. The dissipation rate ε is modeled as

$$\varepsilon = \begin{cases} 2\nu\, k_P/y_d^2 & \text{for} \quad y < y_d \\ k_P^{1.5}/(c_\ell y) & \text{for} \quad y > y_d \end{cases} \tag{3.56}$$

Then, its cell-averaged value $\bar{\varepsilon}$ becomes:

$$\bar{\varepsilon} = \begin{cases} 2\,k_P^2/(\nu y_d^2) & \text{for} \quad y < y_d \\ \dfrac{1}{\nu}\dfrac{k_P^2}{y_n^*}\left[\dfrac{1}{y_d^*} + \dfrac{1}{c_\ell} log\ (y_n^*/y_d^*)\right] & \text{for} \quad y > y_d \end{cases} \tag{3.57}$$

where the characteristic dissipation length y_d^* is $2c_\ell$.

3.2.5 The Extended forms of the Analytical Wall Function:

Although the assumptions used in the AWF are still semi-empirical, the assumptions are less restrictive than the conventional WF models. It is possible to introduce further refinements to the AWF to expand the range of flows that it can be applied to. The AWF has several extended forms for different kinds of flows such as gas/liquid interface and rough wall. This study used three extended forms, α function type, wall normal component and laminarization factor.

(a) α function type

Suga and Ishibashi [16] researched the effects of α, growth ratio of the eddy viscosity in the wall-adjacent cell. The original AWF regards α to be a constant, $\alpha = c_\ell c_\mu = 2.55 \times 0.09$. On the other hand, the extended AWF regards α as a function of cell-averaged strain ratio $\bar{S}$.

$$\alpha = c_\mu[1.6 + 1.9\{-(f_s\bar{S}/5)^{1.5}\}], \tag{3.58}$$

where f_s is a flatness parameter and a function of turbulent Reynolds number R_{tp}. $\bar{S}$ can be described as:

$$\bar{S} = \frac{1}{y_n}\int_0^{y_n} \tau\sqrt{S_{ij}S_{ij}/2}dy, \tag{3.59}$$

$$f_s = 1 - 0.7\exp\{-(R_{tp}/40)^2\}, \tag{3.60}$$

where $S_{ij} = \partial U_i/\partial x_j + \partial U_j/\partial x_i, \tau = \mathrm{k}/\varepsilon,$ and $R_{tp} = k_P^2/(\nu\varepsilon_p)$.

(b)Wall-normal component

The second modification to the AWF includes a convection term for the wall normal direction. Convection in the wall normal direction may not be negligible at stagnation points. Therefore it may improve results by including the wall normal conpoment to the original AWF. Mostafa et *al*. [14] discussed the issue, and concluded that including the wall normal convection term to the energy equation was the most effective way and including it to momentum equations was relatively minor effect. Therefore, this study also included the wall normal convection term only to the energy equation. The modified convection term of the energy equation is

$$C_T = \frac{\nu^2}{k_P}\left[\rho U\frac{\partial\theta}{\partial x} + \rho V\frac{\partial\theta}{\partial y} - S_\theta\right], \tag{3.61}$$

where the modeled wall normal velocity V is quadric variation in the sub-layer and piecewise linear variation above the layer as shown in *figur3.4.* The value of $\rho V\frac{\partial\theta}{\partial y}$ is calculated using numerical integration. The number of partitions is twenty, which is the same with turbulence energy.

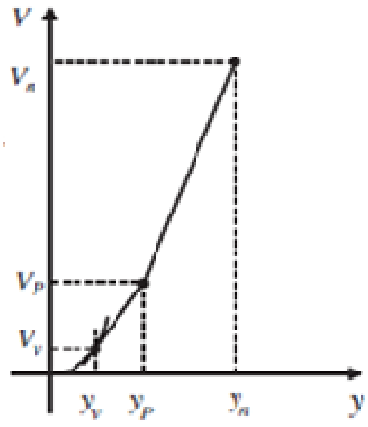

Figure 3.4: V profile in the modified AWF.

(c) Laminarization factor

The final modification to the AWF is called the laminarization effect, which was discussed by Gerasimov et al. [15]. They expressed this effect by modifying the cell-averaged epsilon term,

$$\bar{\varepsilon}_{new} = f_{\varepsilon}\bar{\varepsilon}_{original} \tag{3.62}$$

$$f_{\varepsilon} = \begin{cases} 1 + 1.5\{1 - \exp[-6.9(\lambda - 0.98)]\} \\ \qquad \{1 - \exp[-193\max(\alpha_{\lambda}, 0))^2]\} \end{cases} \text{for} \quad \lambda < 1$$
$$\begin{cases} 1 - 0.25\{1 - \exp[(1 - \lambda)/\lambda]\} \\ \qquad \{1 - \exp[-11.1\max(\gamma_{\lambda}, 0))^2]\} \end{cases} \text{for} \quad \lambda \geq 1 \tag{3.63}$$

where,$\lambda = \tau_w/\tau_v = \mu\sqrt{(\partial U/\partial y)^2}\big|_{y=0}/\mu\sqrt{(\partial U/\partial y)^2}\big|_{y=y_v}$, $\alpha_{\lambda} = \lambda/1.02 - 1$,and $\gamma_{\lambda} = 0.98/\lambda - 1$.

CHAPTER 4: RESULTS and DISCUSSION

4.1 **Computational condition:**

Figures 4.1 and 4.2 show the outline of the test section with a coordinate system and the computational grids used for the intermediate level Reynolds number case (Re=60,000). This study employed structured grids and a multi-block method. In order to hold the best condition, the first node points were basically set at $y^+ > 30$ from the closest wall for the WF models and $y^+ < 1$ for the LRN model. Grid dependencies were tested using twice denser grids (first layer thickness did not change). *Table* 4.1 shows grid numbers employed to investigate the dependencies. The grid dependencies were evaluated using Nusselt number profiles on the centerline of the heated wall as shown in *figures* 4.3-4.5.

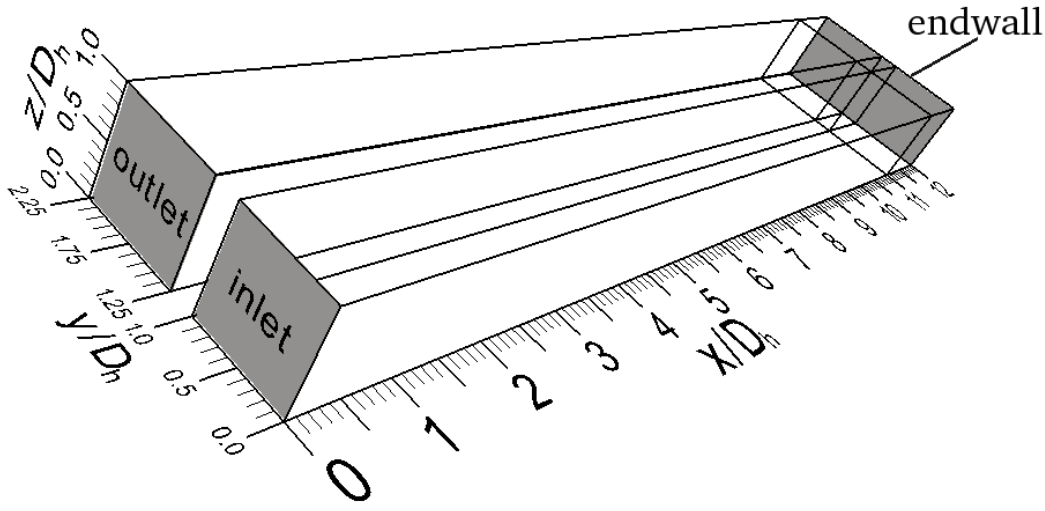

Figure 4.1: Outline of the test section.

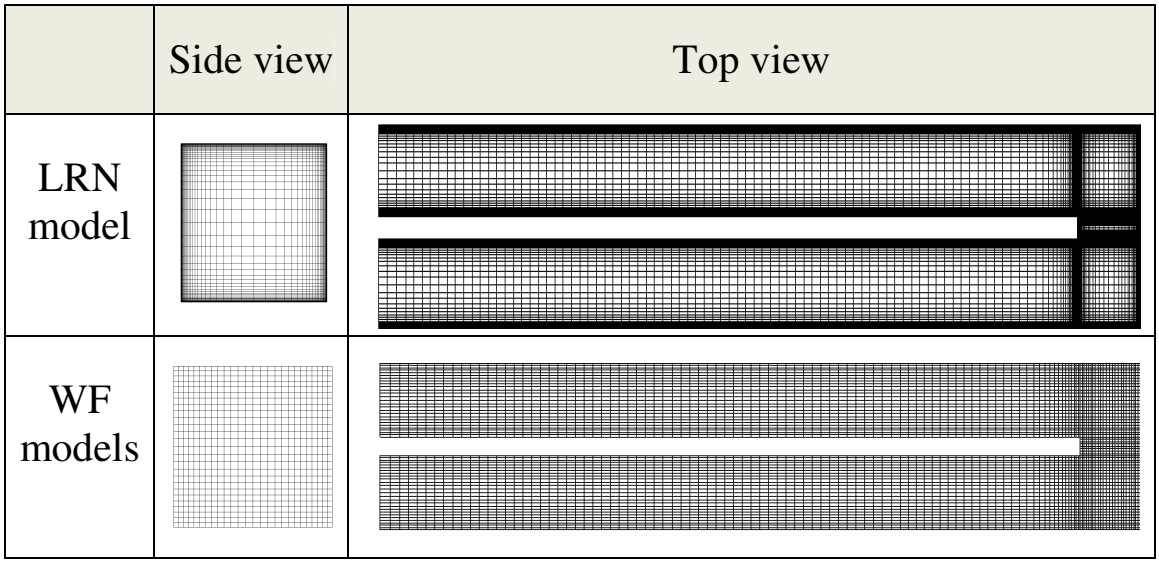

Figure 4.2: Computational grids.

Table 4.1: Grid numbers employed in the calculations.

Reynolds Number	WF models		LRN model	
	grid1	grid2	grid1	grid2
30,000	130,000	235,000	1,333,000	2,817,000
60,000	186,000	352,000	2,453,000	5,753,000
90,000	207,000	586,000	2,880,000	6,940,000

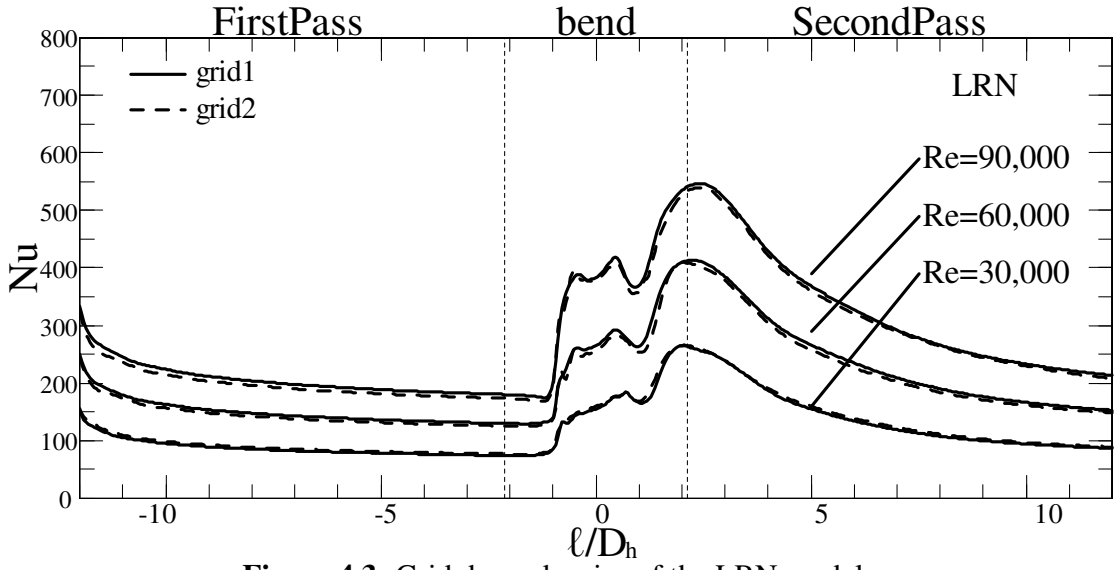

Figure 4.3: Grid dependencies of the LRN model.

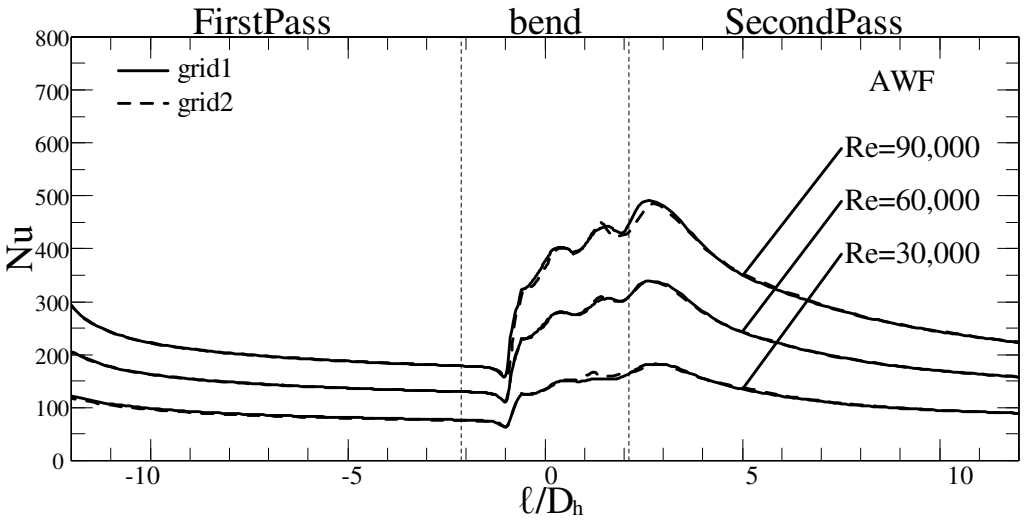

Figure 4.4: Grid dependencies of the AWF model.

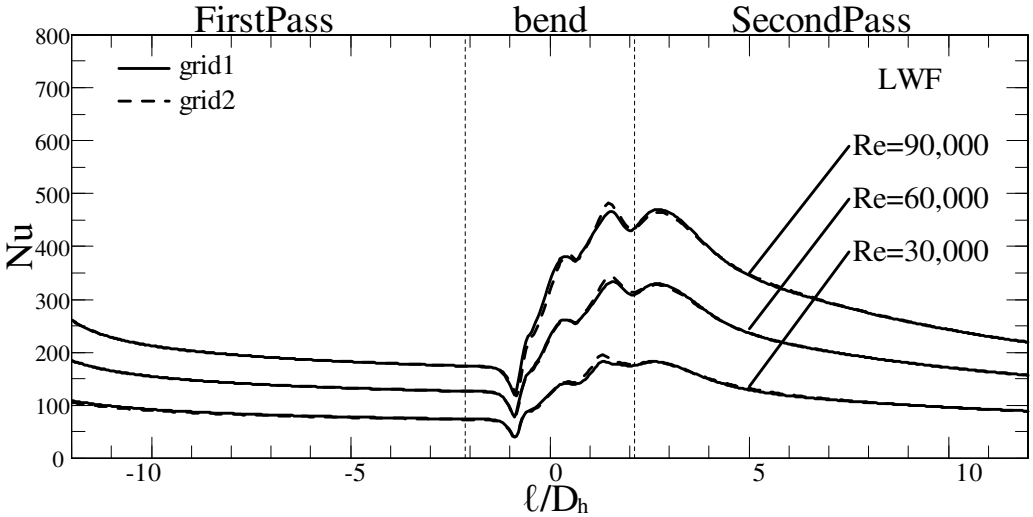

Figure 4.5: Grid dependencies of the LWF model.

Basically, there were comparatively low differences between both grids except for the bend region where relatively high differences of about ten percent were observed. However, since the high differences were observed only at several points, this study employed the grid1. It also can be seen from *table* 4.1 that the WF models were able to save more than 90% grids of the LRN model.

4.2 **Validations of the turbulence models:**

This study used Nusselt number profiles on the centerline of the heated wall for validations of the turbulence models. *Figures* 4.6- 4.8 show the comparison of measured and calculated Nusselt number profiles. As can be seen, the turbulence models predicted Nusselt number profiles in reasonable range. Then, this study concluded the turbulence models were validated. Further discussions of the thermal predictions will be described after section 4.5.

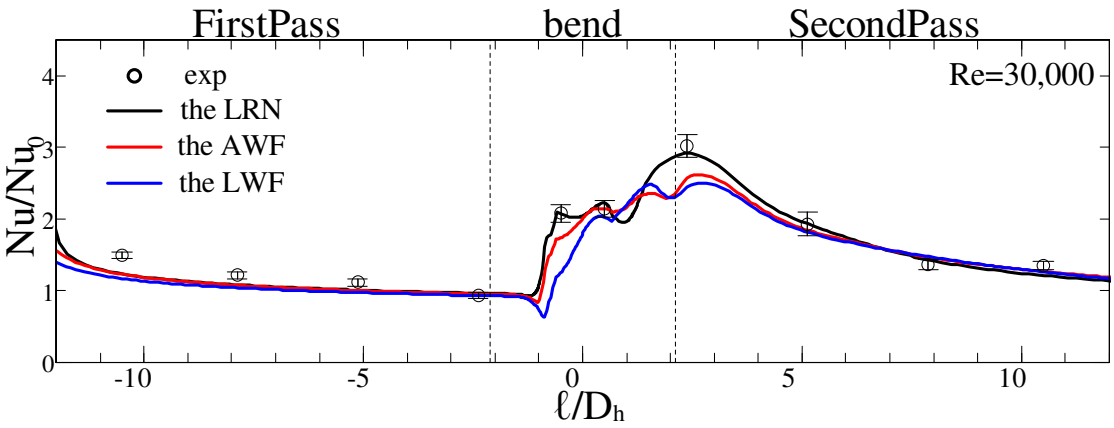

Figure 4.6: Model validations (Re=30,000).

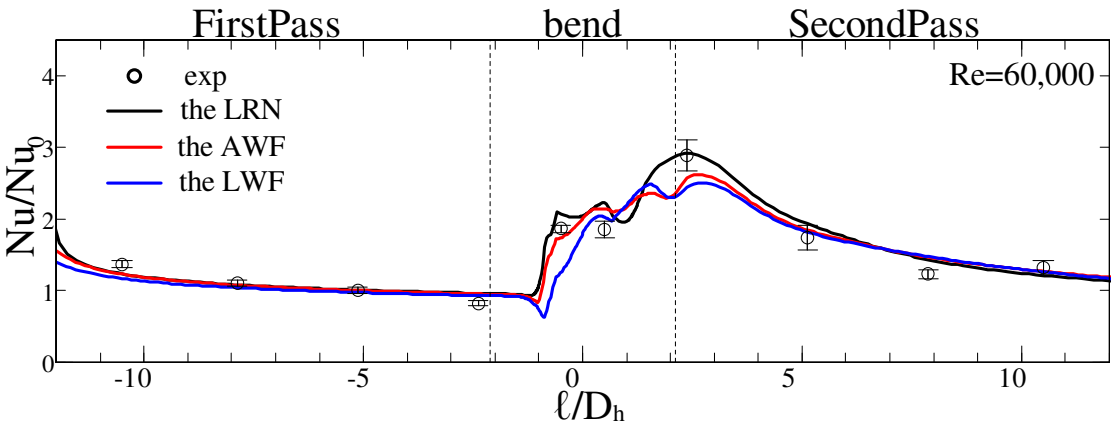

Figure 4.7: Model validations (Re=60,000).

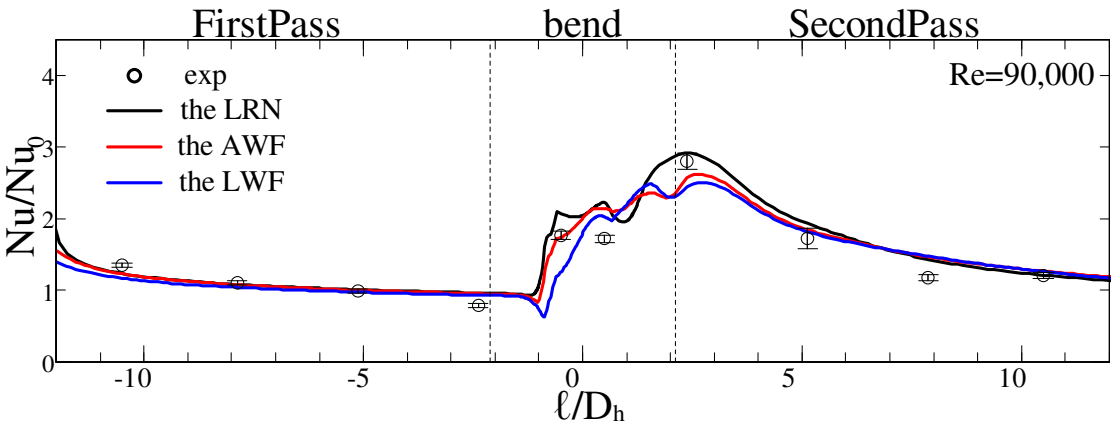

Figure 4.8: Model validations (Re=90,000).

4.3 **Velocity field:**

Figure 4.9 shows velocity vectors on velocity magnitude contours in the bend region on each x-y plane (z/D_h=0.5, z/D_h=0.3, z/D_h=0.1) and *figure 4.10* shows velocity vectors and velocity magnitude contours on each y-z plane (x/D_h=11.5, x/D_h=10.0, x/D_h=8.0, x/D_h=6.0) for the intermediate Reynolds number case (Re=60,000). As can be seen, the predicted flow patterns are similar among the LRN model, the AWF and the LWF. However, the LRN model predicted a separation position at location further downstream than the WF modes in the first pass and a reattachment point at a position further upstream in the second pass. It also can be seen that the fluid entering the turn from the inlet impinges on the end wall, and after the turn, it impinges on the outer wall in the second pass again. These impingements produced a high heat transfer enhanced region (see *figure* 4.18). The turn also enhanced secondary flows in the second pass. While slight secondary flows occur in the first pass, there are strong secondary flows in the second pass.

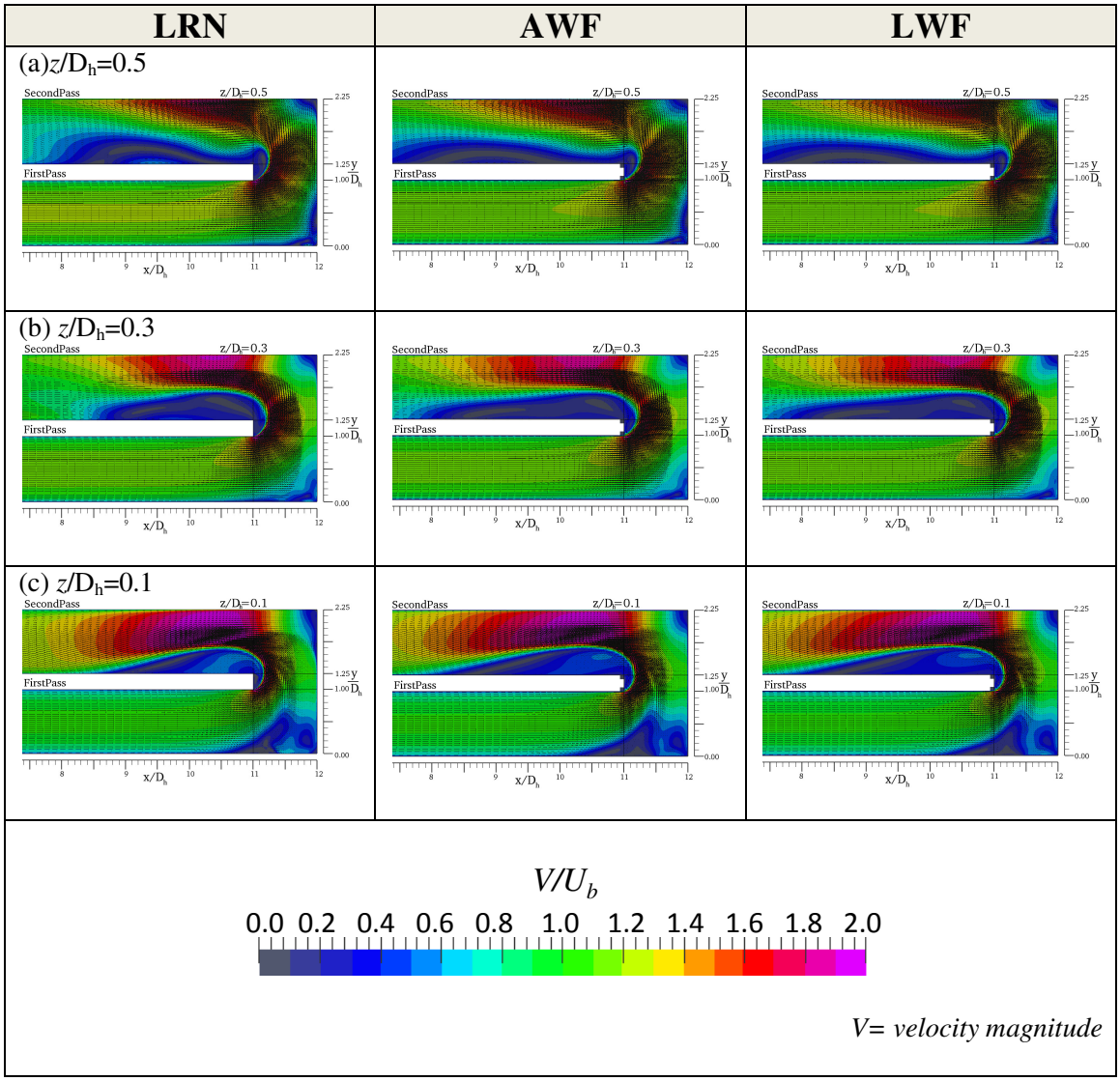

Figure 4.9: Velocity vectors and dimensionless velocity magnitude contour on x-y planes for middle Reynolds case (Re=60,000).

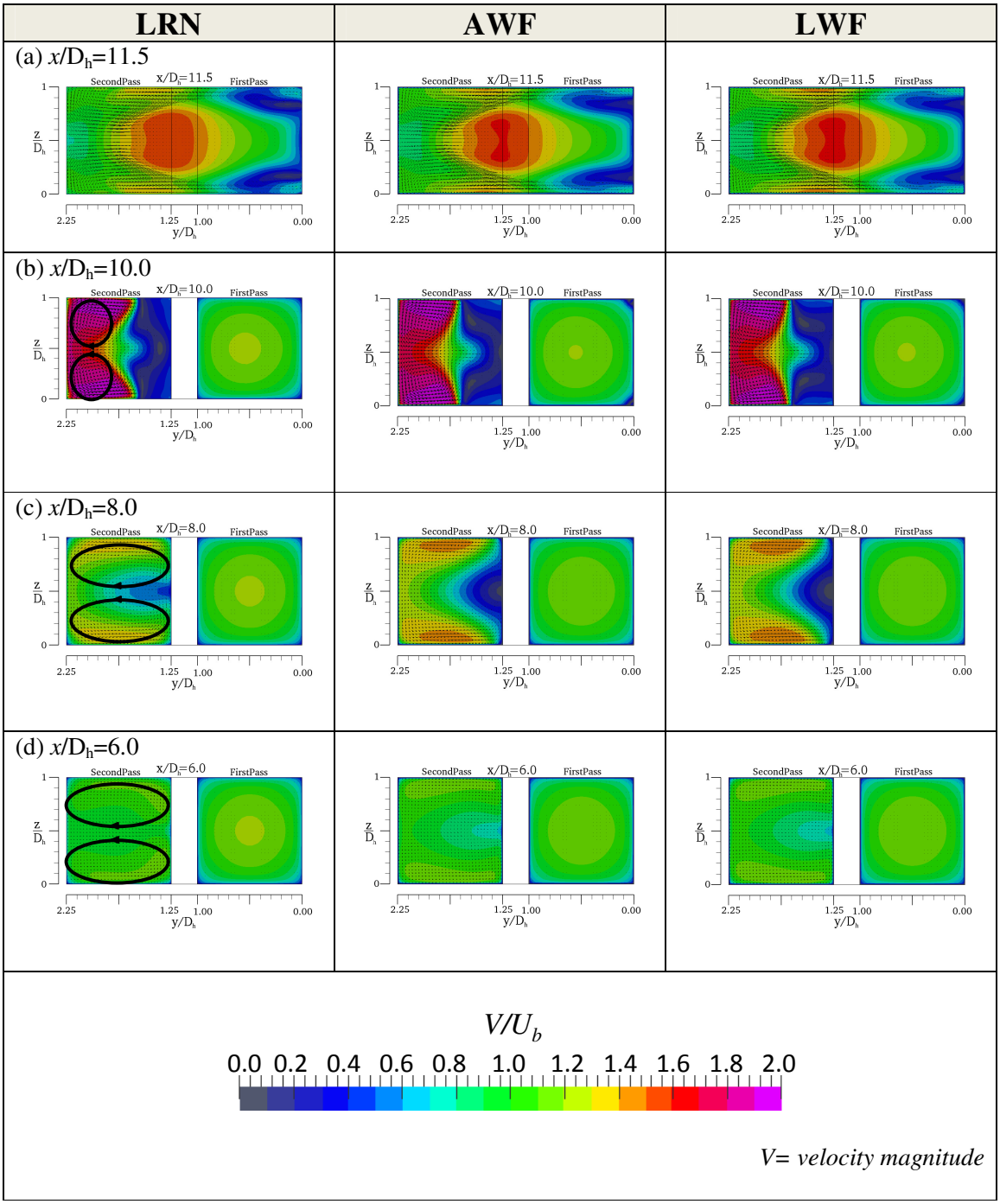

Figure 4.10: Secondary flows and dimensionless velocity magnitude contour on x-y planes for intermediate Reynolds case (Re=60,000).

Figure 4.11 shows locations of the reference lines and *figure* 4.12 shows velocity magnitude, V, profiles on the reference lines. As can be seen, the WF models had good agreement with the LRN model for x/D_h<10 in the first pass and for x/D_h<6 in the second pass. For the other regions, (the turn region: x/D_h>11 in both passes and after the turn region: 6<x/D_h<11 in the second pass) the WF models predicted moderately higher velocities and larger differences can be seen on the inner line in the second pass. Again, the AWF's results were slightly closer to the LRN's results.

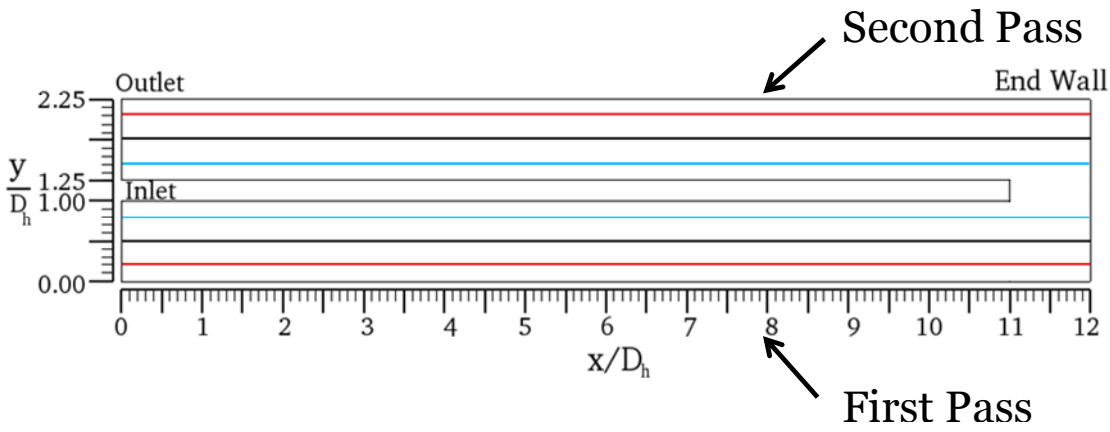

	First pass(y/D_h)	Second Pass(y/D_h)
inner line	0.2	1.45
center line	0.5	1.75
outer line	0.8	2.05

Figure 4.11: Reference lines.

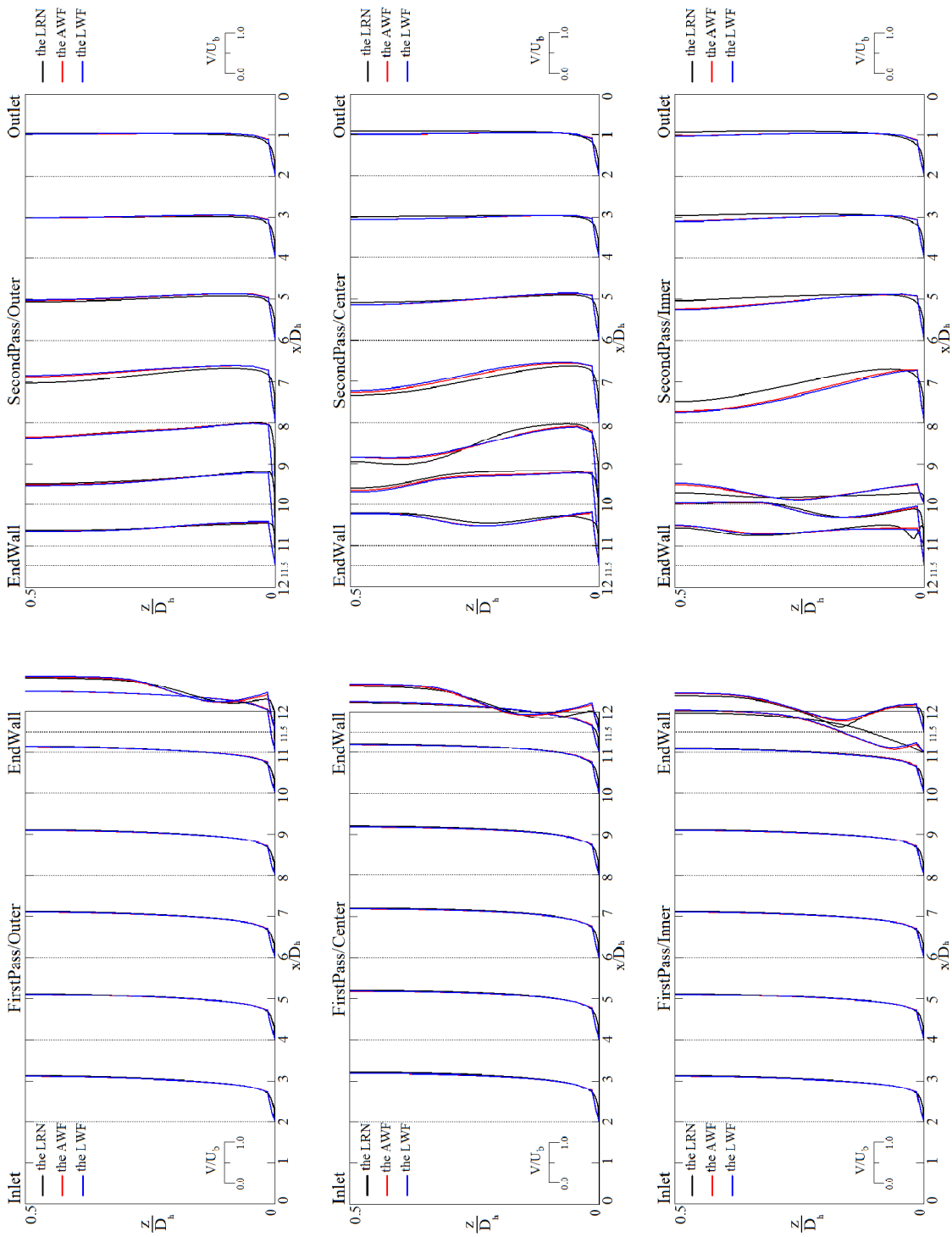

Figure 4.12: Comparison of velocity profiles on the reference lines (Re=60,000).

4.4 **Turbulence field:**

Figure 4.13 shows turbulence energy profiles on the reference lines predicted by each turbulence model (Re=60,000). It can be seen that there was no significant difference for x/D_h<10 in the first pass and for x/D_h<6 in the second pass as well as the velocity predictions. High level of turbulence energy occurred in the bend region and after the turn region (8<x/D_h<12 in the second pass). Fluid flow entering the turn section accelerated with strong secondary flows on the outer half side of the channel because the recirculation region generated after the turn reduced the channel width (x/D_h=10.0 in *Figure* 4.9). The flow then decelerated as it went further downstream, because the reduction of the recirculation region restored the channel width there. The area of strong secondary flows also spread to the whole area at x/D_h=8.0 from the outer half side at x/D_h=10.0. Therefore, at x/D_h=10.0, high turbulence energy was generated on the centerline where steep velocity gradients occurred. At x/D_h=8.0, near the reattachment point, turbulence energy became higher on the inner line. Again, the AWF model showed slightly closer results to the LRN model's results than the LWF.

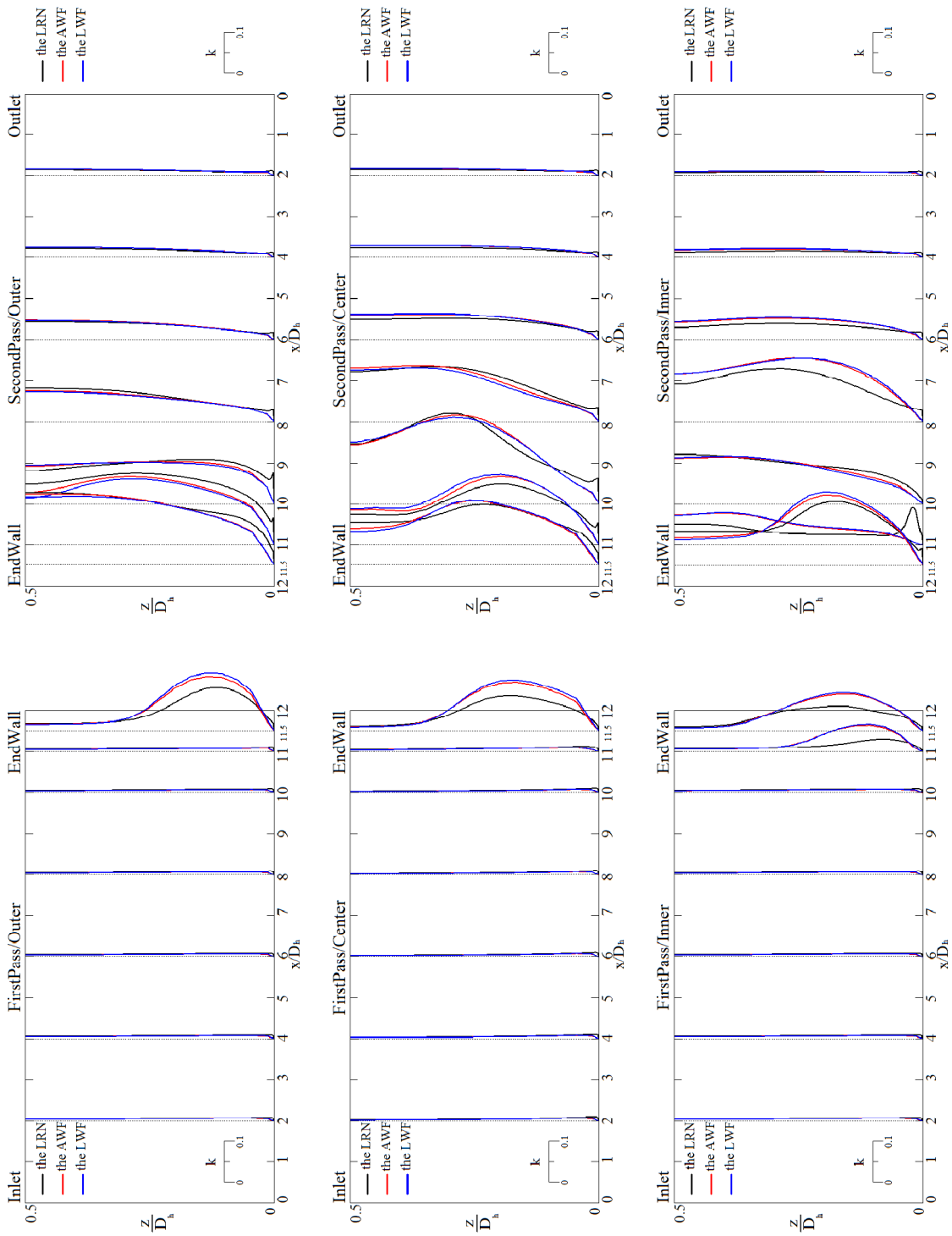

Figure 4.13: Comparison of turbulence energy profiles on the reference lines

(Re=60,000)

4.5 **Thermal field:**

Figure 4.14 illustrates the reference lines and temperature measurement points. To evaluate thermal prediction performance, normalized Nusselt number profiles were used. The Nusselt number was normalized with the Dittus-Boelter equation. *Figures* 4.15-5.17 show comparison of the measured and calculated Nusselt number profiles on the reference lines and *figure* 4.18 shows the Nusselt number distributions computed by each turbulence model. There were larger differences for the Nusselt number predictions, compared with the velocity and turbulence energy predictions. The largest difference can be seen after the bend in the second pass. The LRN model predicted higher Nusselt number than the WF models, and had better agreement with the experimental results.

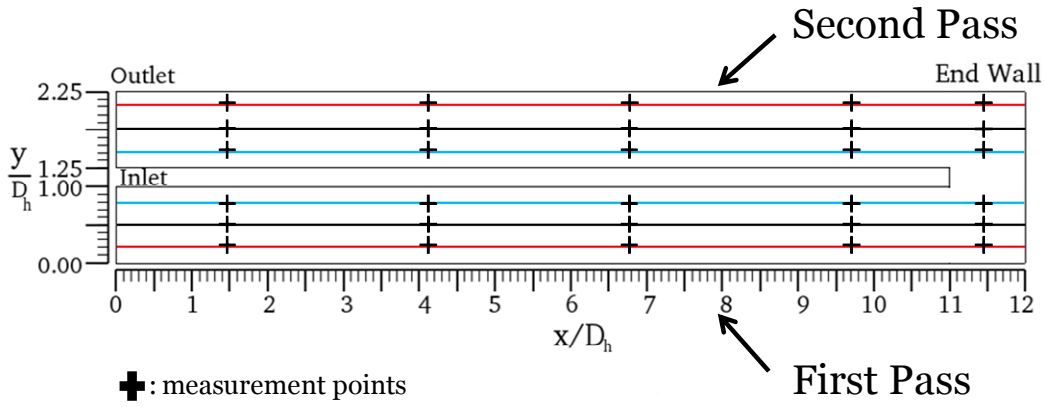

	First pass(y/D_h)	Second Pass(y/D_h)
inner line	0.2	1.45
center line	0.5	1.75
outer line	0.8	2.05

Figure 4.14: Reference lines with measurement points

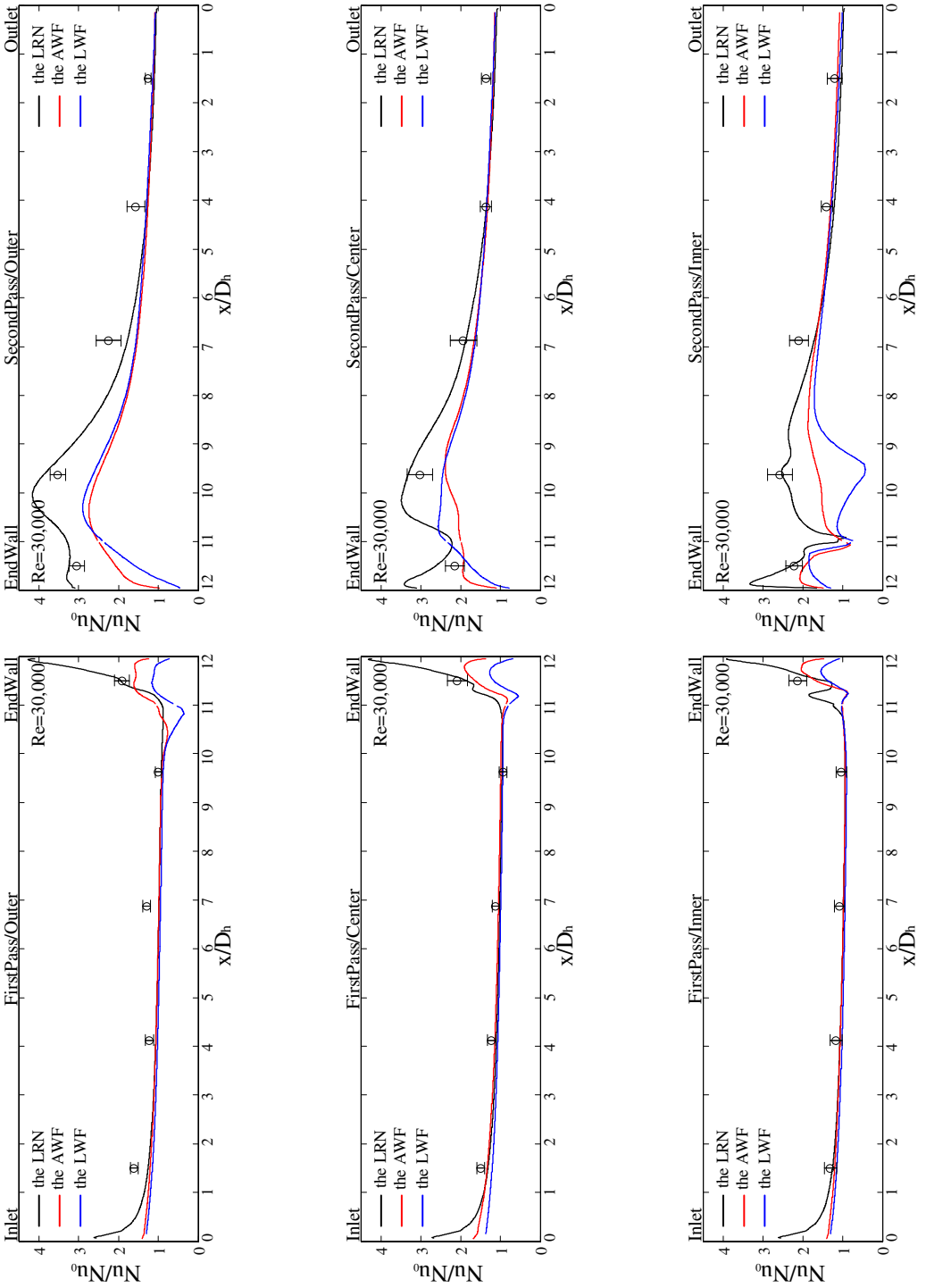

Figure 4.15: Local Nusselt number profiles on the reference lines with the experimental results (Re=30,000).

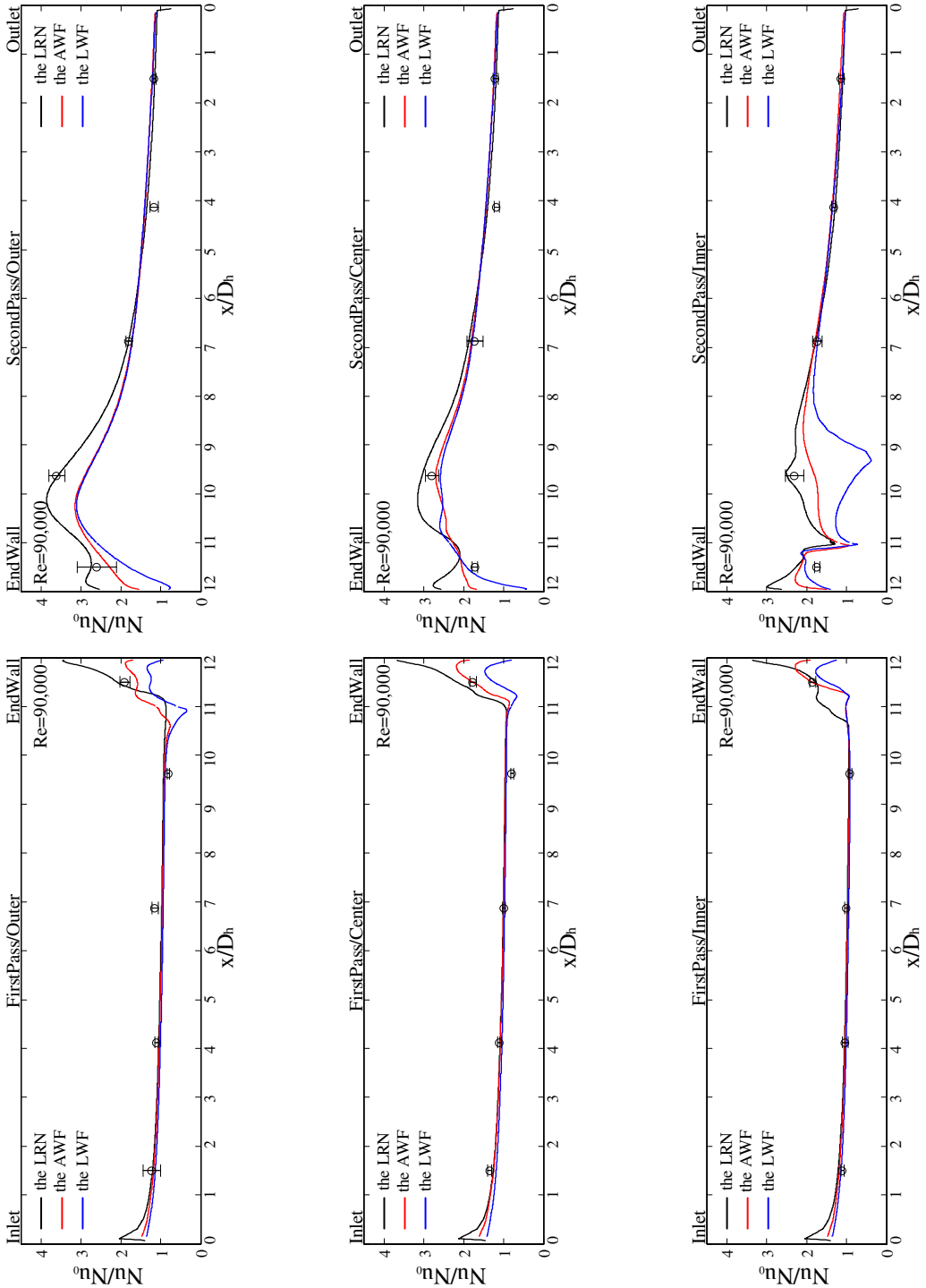

Figure 4.16: Local Nusselt number profiles on the reference lines with the experimental results (Re=60,000).

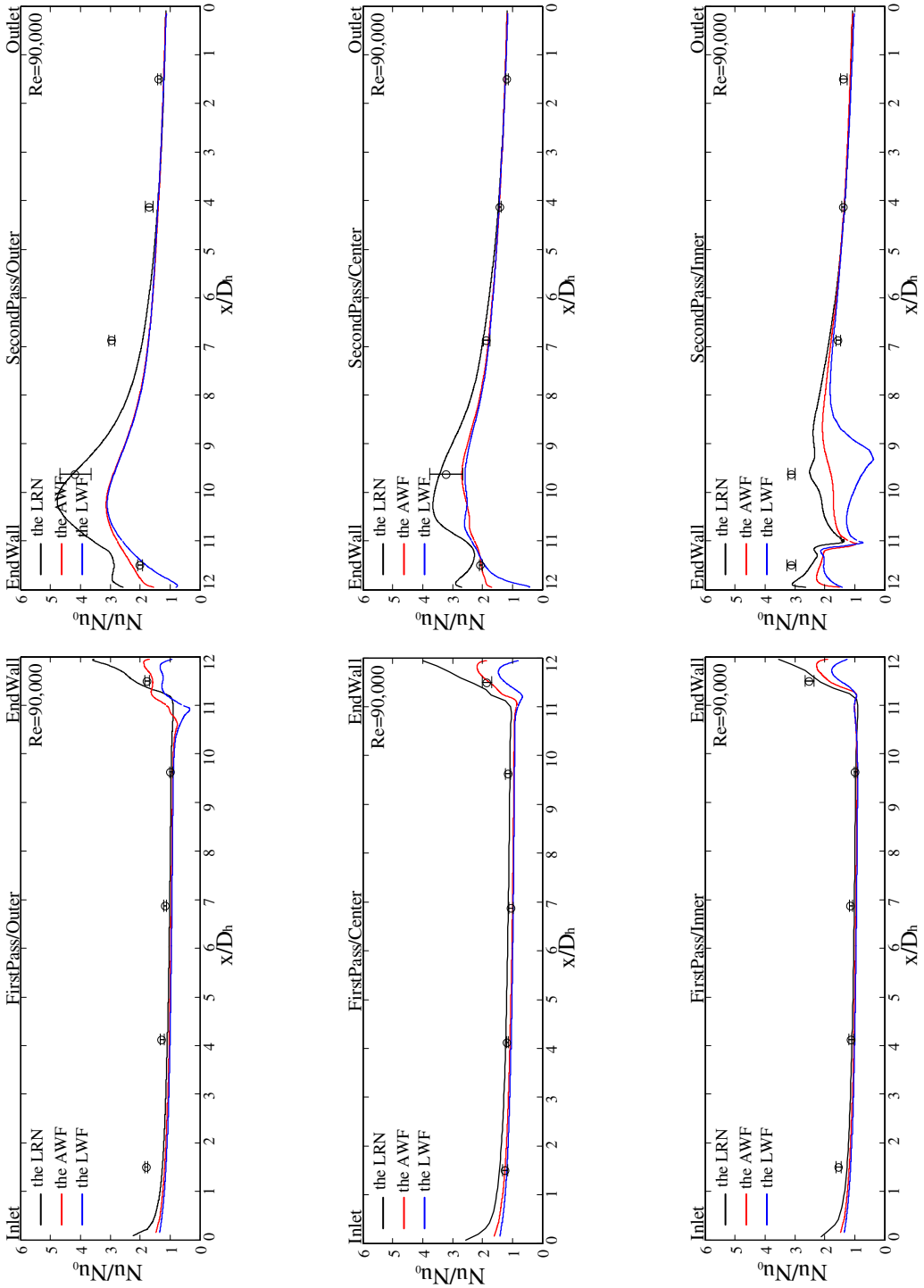

Figure 4.17: Local Nusselt number profiles on the reference lines with the experimental results (Re=90,000).

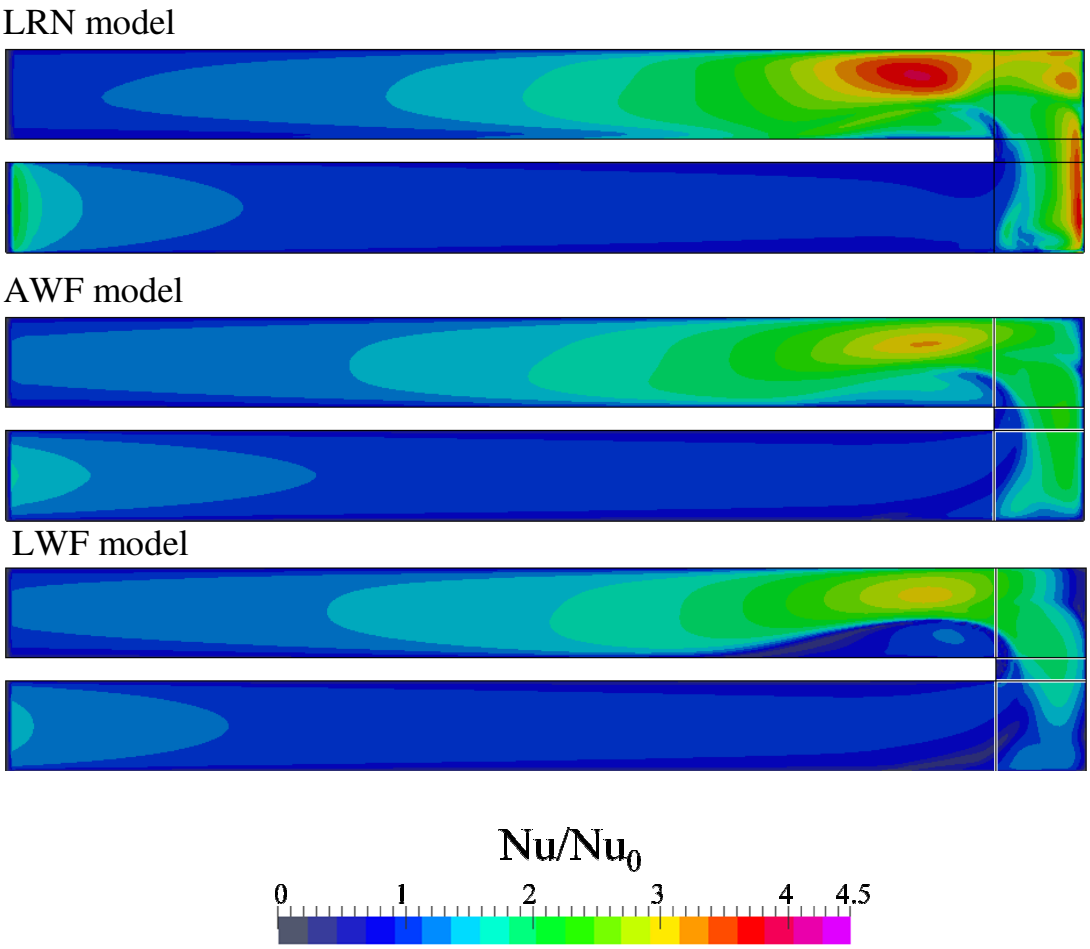

Figure 4.18: Normalized Nusselt number distribution for intermediate Reynolds number case (Re=60,000).

As can be seen in *figure* 4.18, the LWF showed a much lower Nusselt number at the separation and the reattachment regions, because it can be considered that the log-law is impossible in these regions. On the other hand, the AWF predicted more reasonable results in the region, although the predicted Nusselt number was still lower than the LRN model. Considering that the AWF employed thirteen times coarser mesh than the LRN model, however, they are acceptable results.

4.5.1 **Thermal field (the extended forms of the AWF):**

Figures 4.19-4.21 show the predicted Nusselt number profiles on the reference lines using the extended forms of the AWF and *figure* 4.22 shows predicted Nusselt number distributions. First of all, the extended AWF showed minor change. However, the extended forms showed slight changes near the end wall in the first pass and the α function type showed a relatively large Nusselt number in the recirculation region (inner side region for $9.0<x/D_h<11.0$ in the second pass). Again, α function type showed the largest change from the original results among the extended forms. It also predicted a lower Nusselt number for downstream in the second pass ($x/D_h < 8.0$). Since the α function type was developed in two-dimensional geometry condition, it might be necessary to re-tune model parameters used in the AWF form.

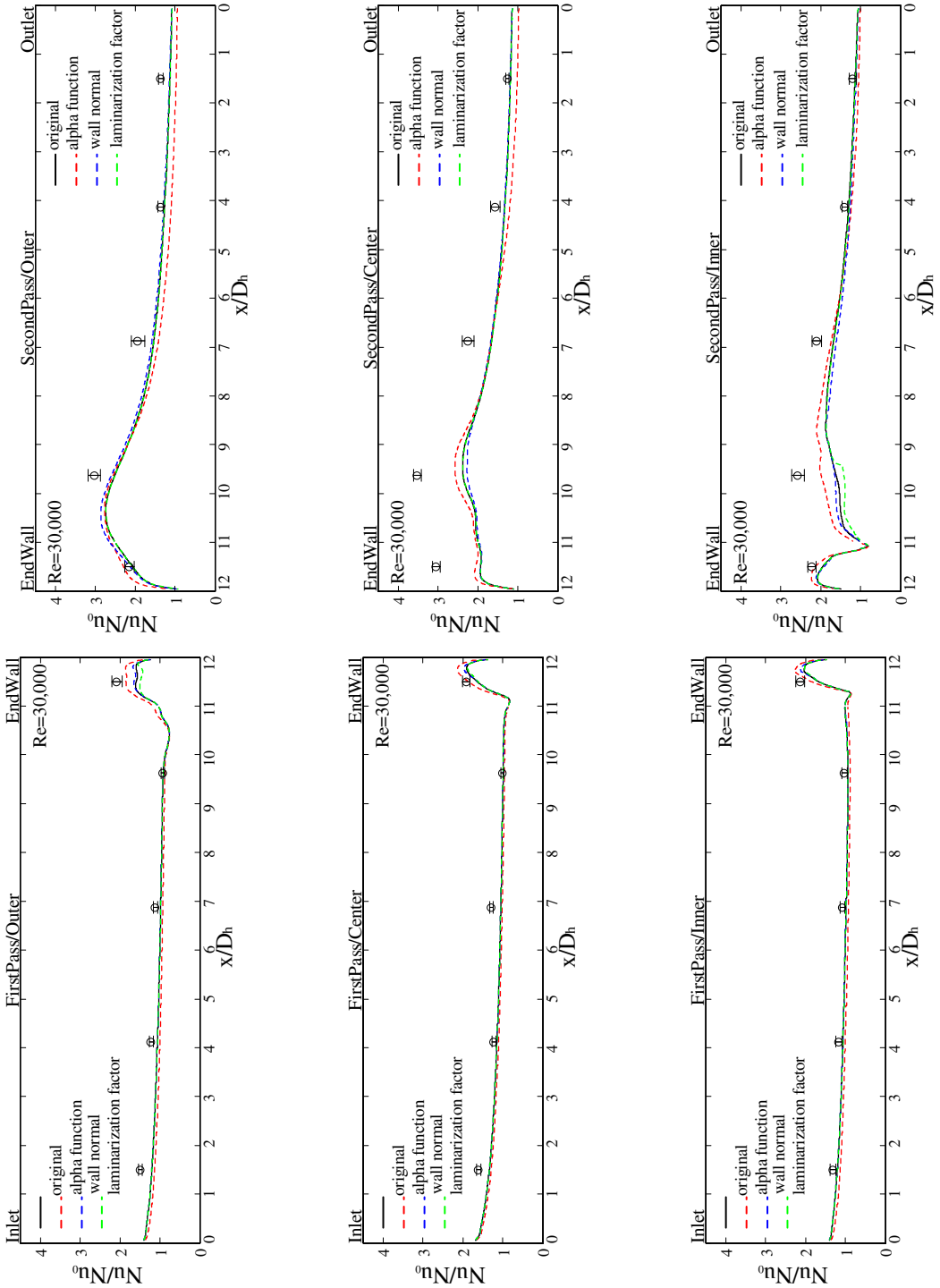

Figure 4.19: Nusselt number profiles of the extended forms of the AWF with the experimental results (Re=30,000).

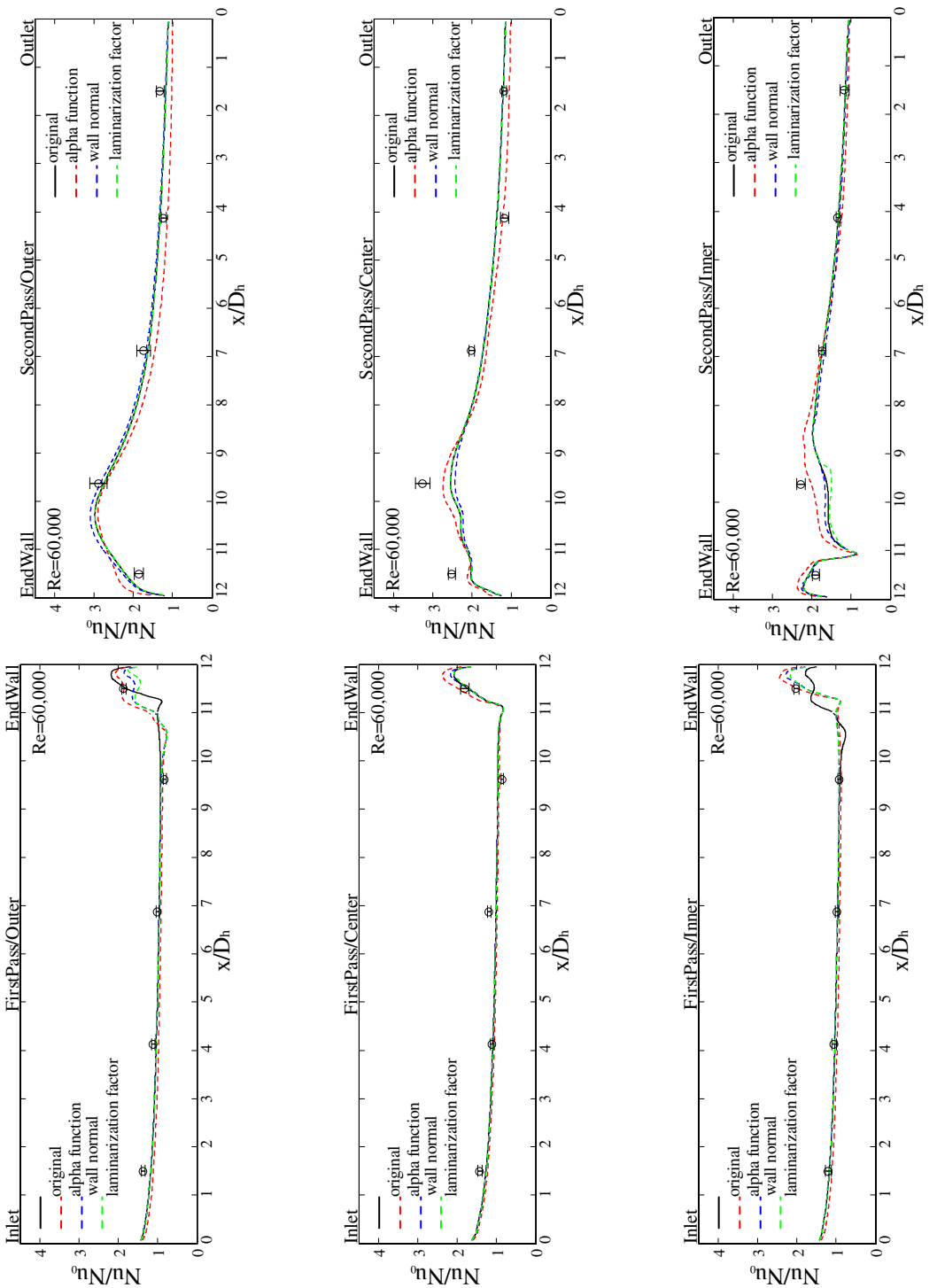

Figure 4.20: Nusselt number profiles of the extended forms of the AWF with the experimental results (Re=60,000).

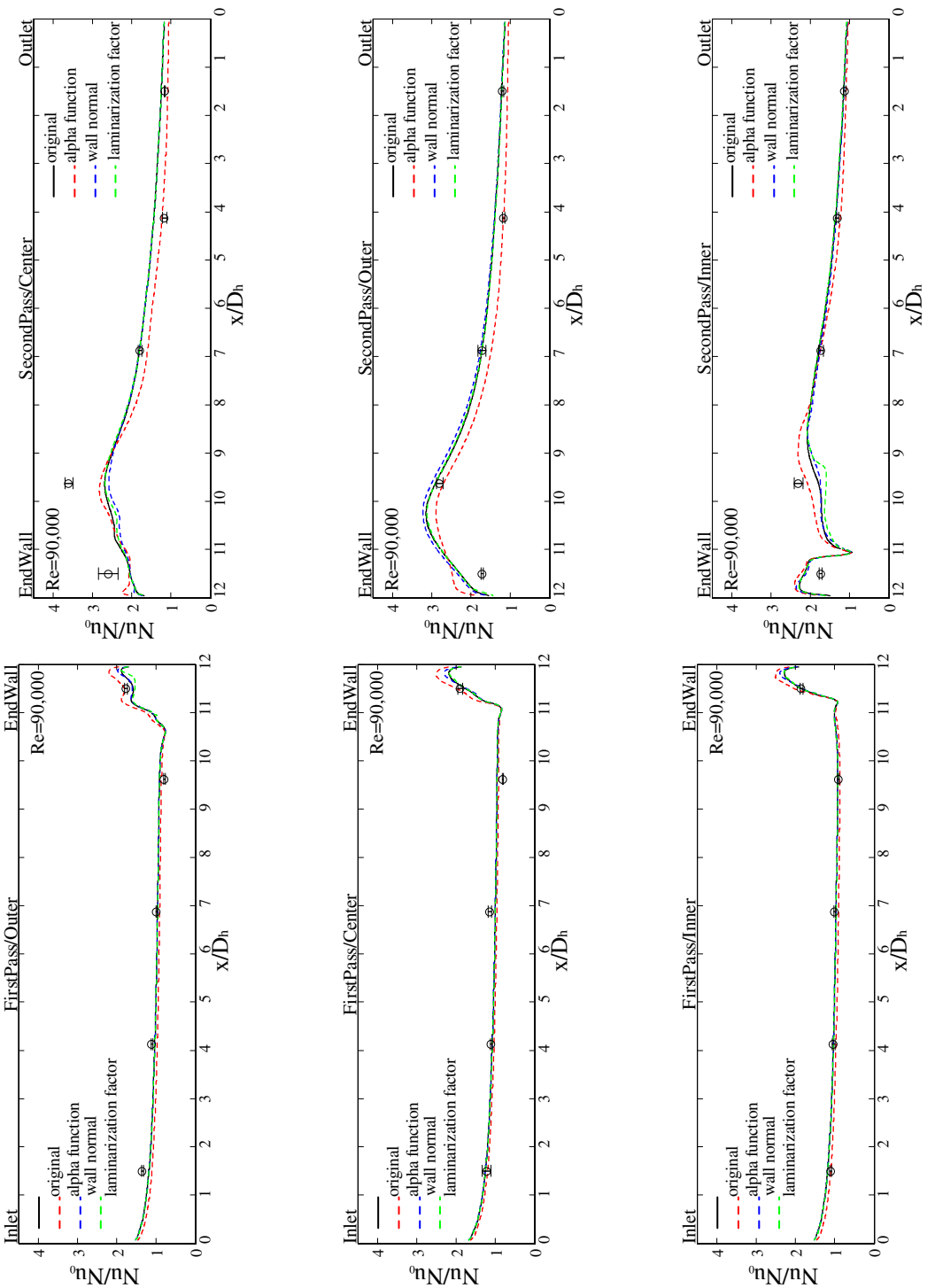

Figure 4.21: Nusselt number profiles of the extended forms of the AWF with the experimental results (Re=90,000).

(a)The Original AWF

(b) α function type

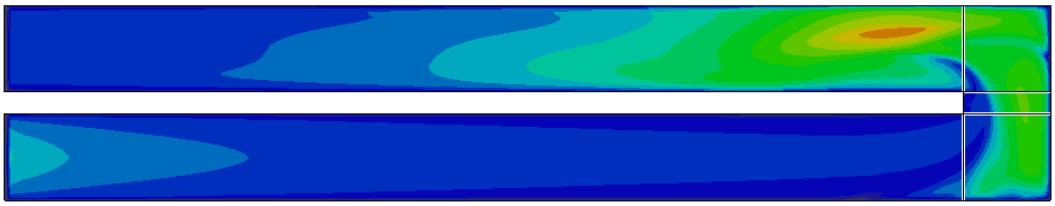

(c) wall normal component

(d) laminarization factor

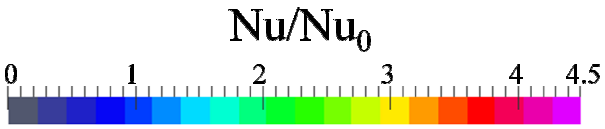

Figure 4.22: Nusselt number distributions predicted

by the extended forms of the AWF with the original AWF (Re=60,000).

4.5.2 **Thermal field (First layer thickness effect):**

The AWF was developed as not only a more reliable but also a more universal wall function model. The LRN models recommend the first layer thickness is less than unity and the conventional WF models recommend that it is between 30 and 300 as shown in *figure* 4.23. The AWF can perform like LRN model thanks to the assumption of zero eddy viscosity if the node point of the wall-adjacent cell is inside the viscous sub-layer. Therefore, The AWF can cover the applicable region of both turbulence models. *Figures* 4.24-4.26 show Nusselt number profiles with different the first layer thicknesses. Solid lines denote Nusselt numbers and dash lines denote corresponding first layer thicknesses. The first layer thicknesses are shown as $y^{+,}$ although the AWF usually employs y^{*}. From these pictures, it can be seen that as the first layer thicknesses became thinner, the resultant Nusselt numbers became higher for $x/D_h > 11.0$ in the first and the second pass and for $x/D_h > 8.0$ in the second pass. For the other region, the AWF showed almost the identical results. Thus, it can be seen that the AWF showed no first layer thickness dependency for simple flow region, although it is in the buffer region. *Table* 4.2 shows the number of node points generated for each mesh. Mesh3 (the finest mesh) was about twice denser than mesh1 which was used to compare with the LWF and LRN models.

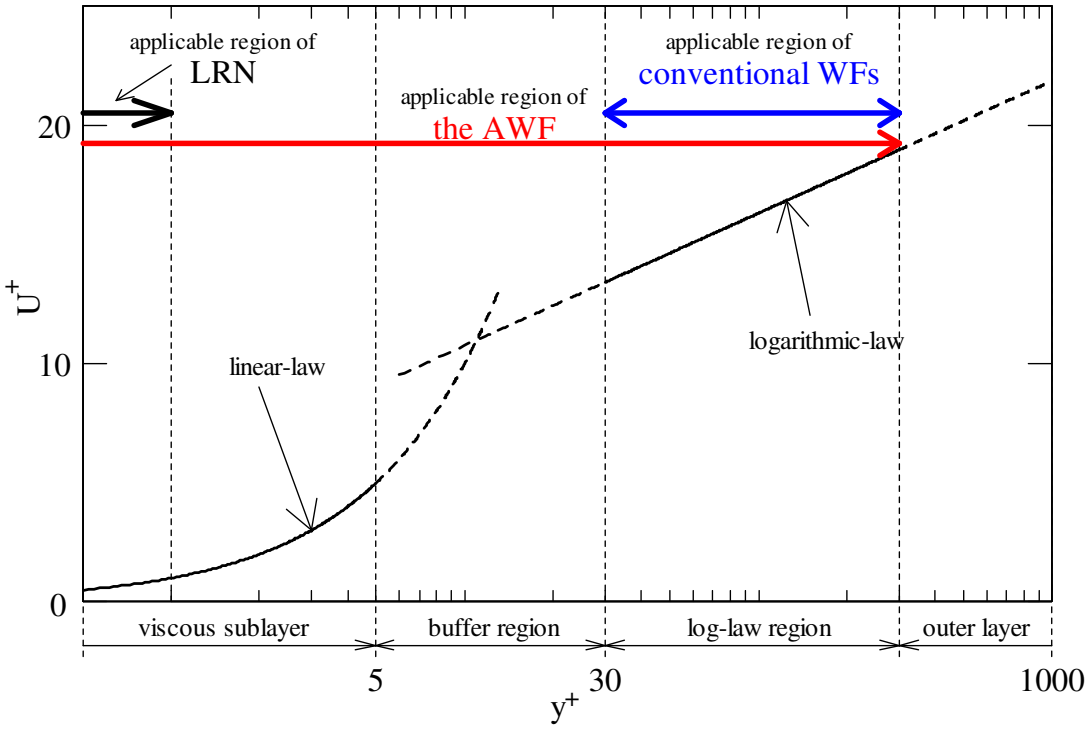

Figure 4.23: Applicable regions of the fist layer thickness.

Table 4.2: The number of node points used in each mesh

Reynolds number	Mesh 1	Mesh2	Mesh3
30,000	130,000	207,000	212,000
60,000	186,000	214,000	336,000
90,000	207,000	212,000	352,000

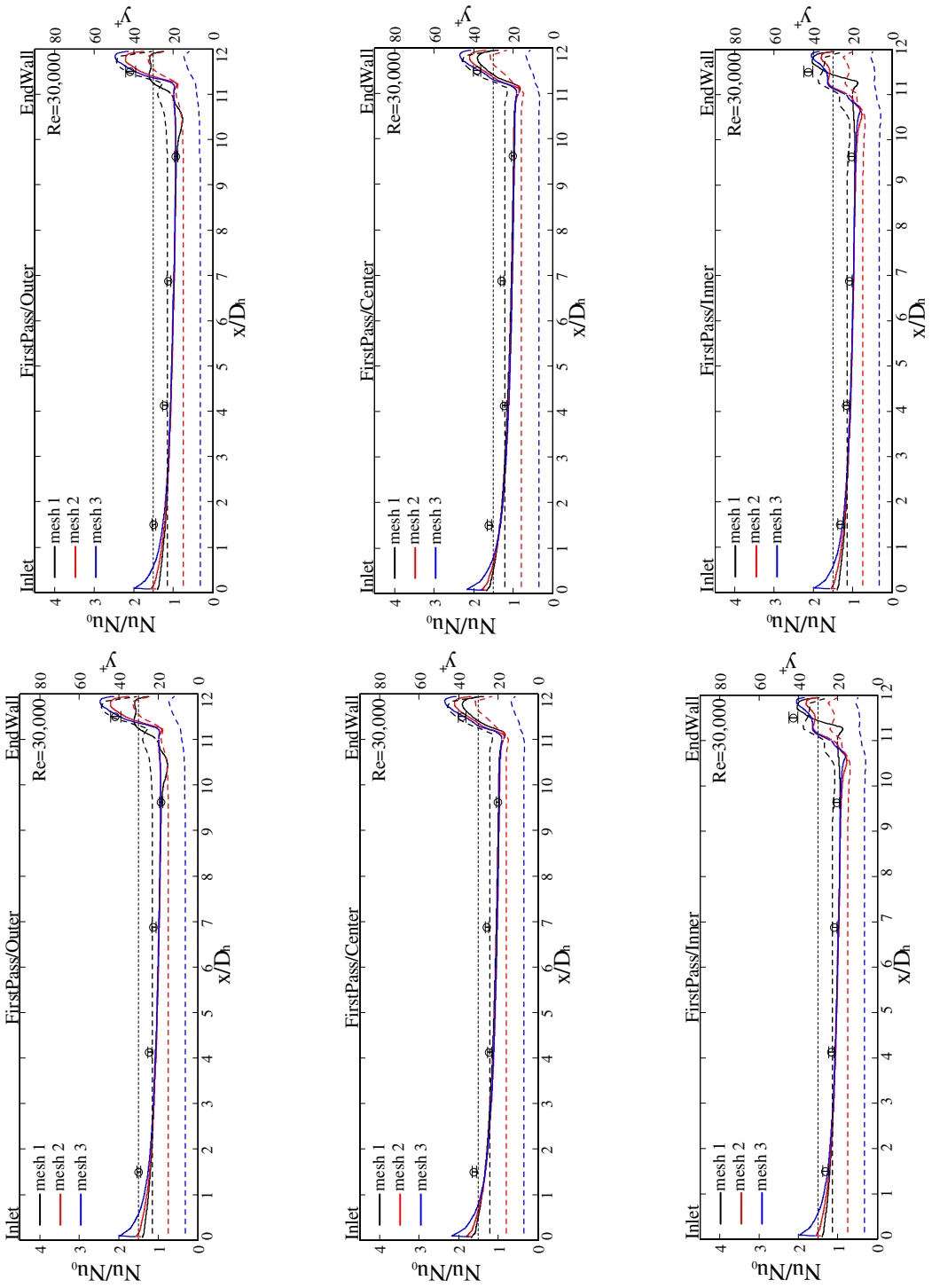

Figure 4.24: Normalized Nusselt number profiles on the reference lines with different first layer thicknesses (Re=30,000).

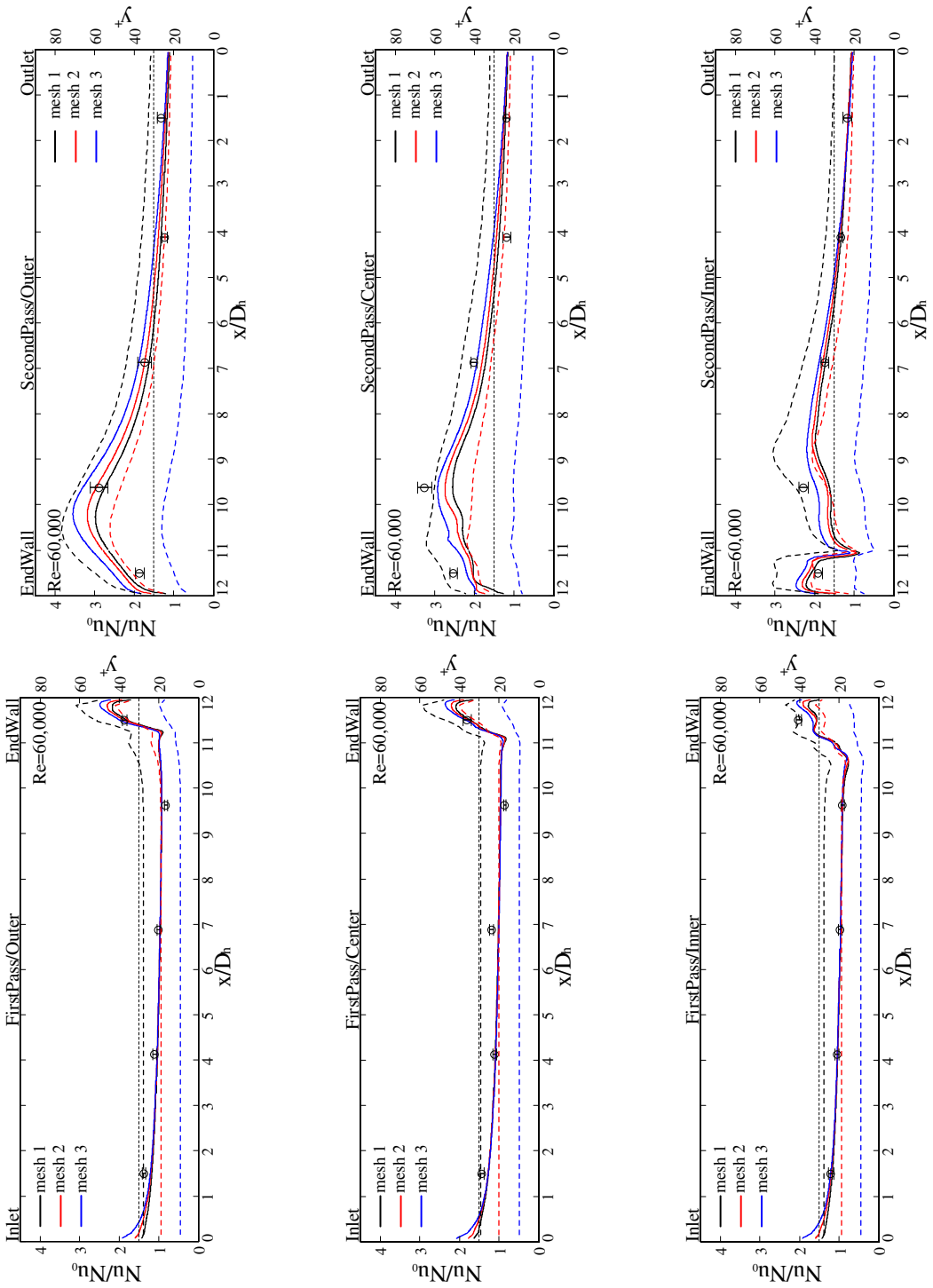

Figure 4.25: Normalized Nusselt number profiles on the reference lines with different first layer thicknesses (Re=60,000).

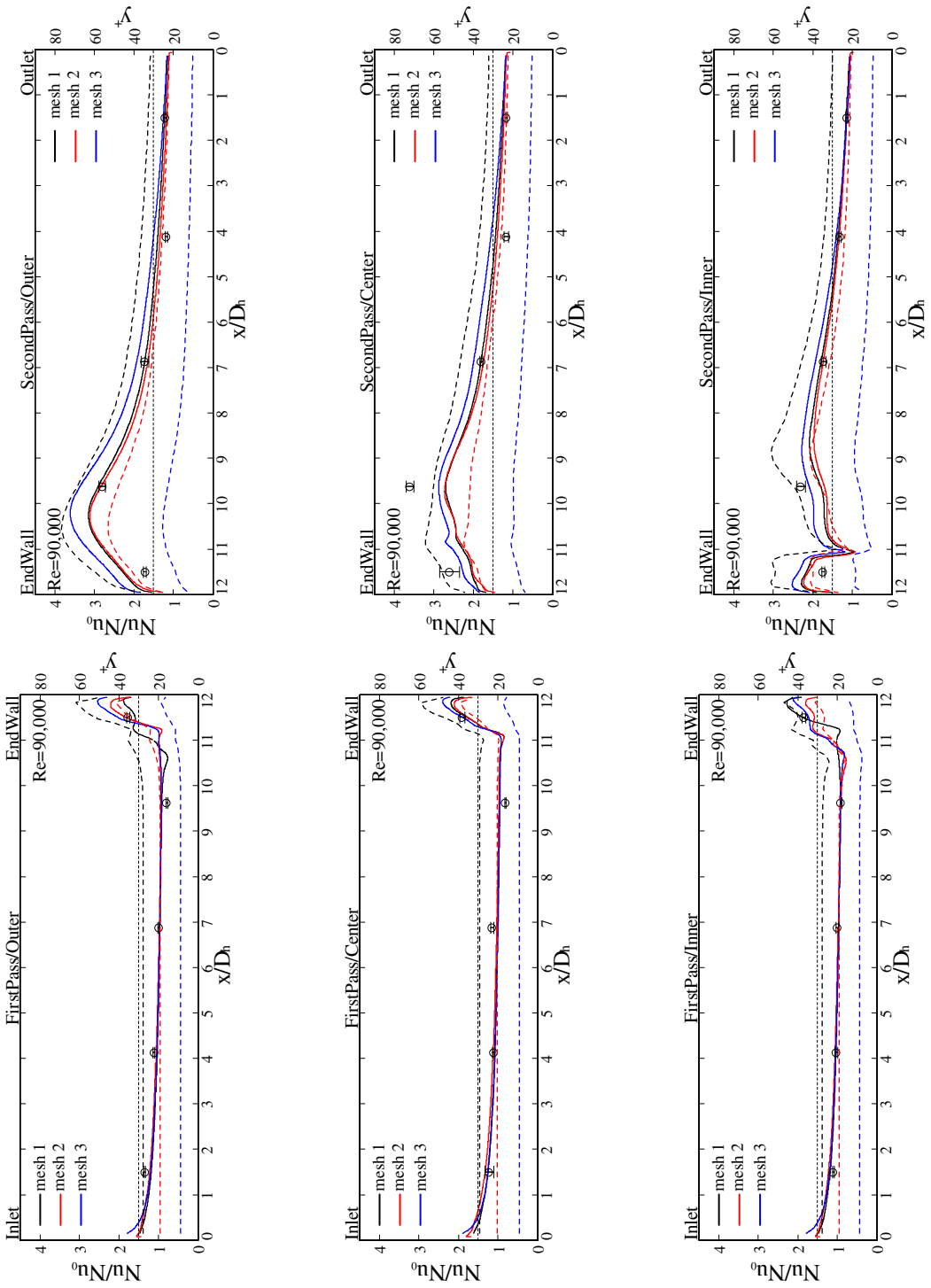

Figure 4.26: Normalized Nusselt number profiles on the reference lines with different first layer thicknesses (Re=90,000).

4.5.3 **Thermal field (the YAP correction effect):**

Figure 4.27 and 4.28 show the YAP correction effect for different first layer thicknesses. The AWF used the LS model to solve the core region. Since the LS model recommends use of the YAP correction, this study also investigated this effect. As can be seen, there was a slight effect for mesh 1. On the other hand, the YAP correction had an effect on the Nusselt number profile for mesh 3. *Figure* 4.29 shows the YAP correction profile on a cross section center line of a square duct calculated by the LS model. As can be seen, the YAP correction has an effect for $y^+<30$. Thus, it is recommended using the YAP correction for the AWF when the first layer thickness y^+ is less than 30.

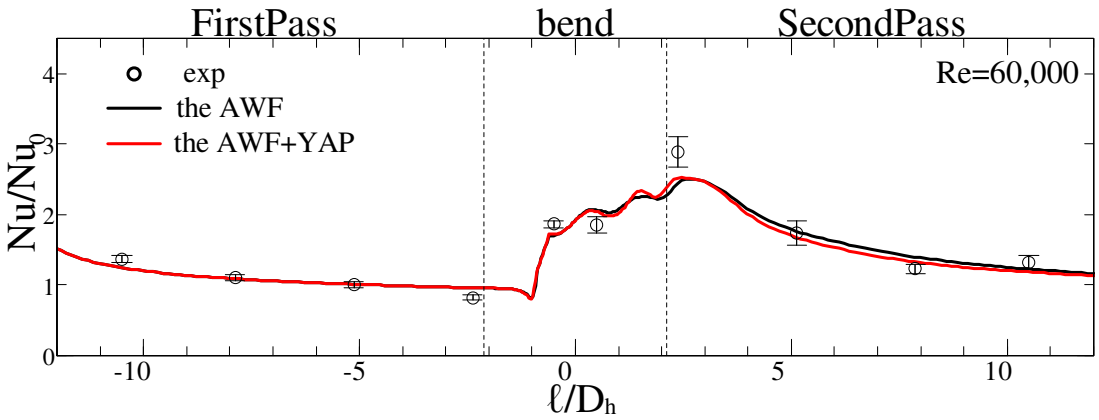

Figure 4.27: The YAP correction effect on Nusselt number profile on the center line for mesh1

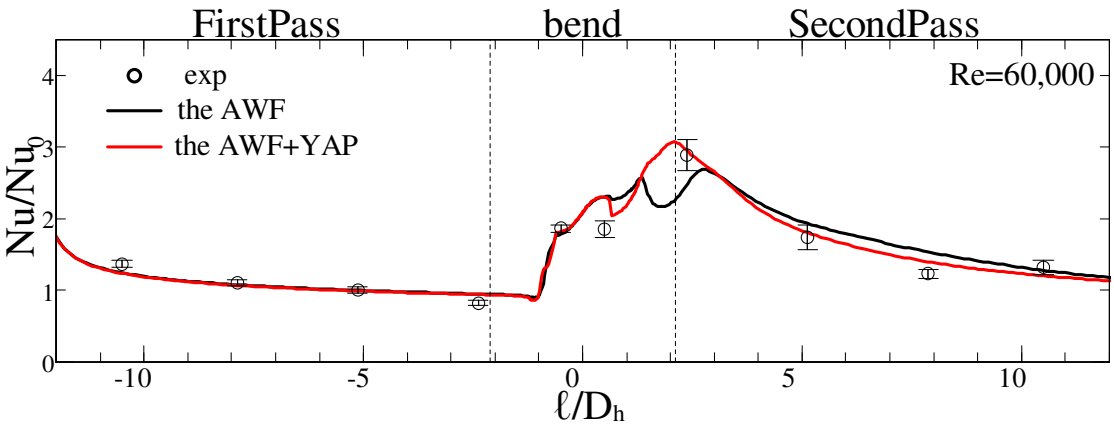

Figure 4.28: The YAP correction effect on Nusselt number profile on the center line for mesh3

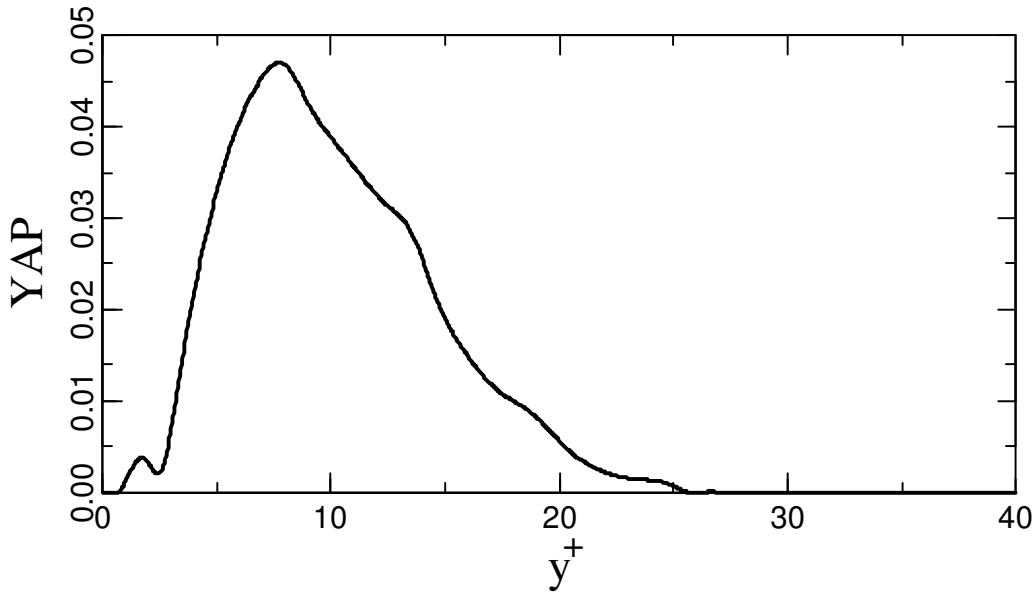

Figure 4.29: The YAP correction profile on a cross section center line of a square duct.

4.5.4 **Thermal field (summary):**

This subsection summarizes the performance of the thermal prediction by using relative error from experimental results. *Table* 4.3 shows the performance of each turbulence model. Among the turbulence models, the LRN model showed the highest accuracy. But it also consumed thirteen times denser mesh than the WF models as stated above (see *table* 5.1 for detailed numbers). The AWF improved thermal field prediction by 31.2%, using the same mesh the LWF model used. *Table* 4.4 shows the performance of each extended AWF model. It can be seen that there was no significant difference among the extended AWFs and the extended forms showed slightly worse results. *Table* 4.5 shows the performance of the AWF with different first layer thicknesses. From *table* 4.3 and 4.5, it can be observed that the AWF performance increases as the mesh becomes finer.

Table4.3: Each turbulence models' performance

Reynolds number	LRN model[%]	The AWF[%]	The LWF[%]
30,000	11.38	15.18	21.08
60,000	8.98	8.57	13.47
90,000	8.62	9.06	13.19
AVERAGE	9.66	10.94	15.91

Table4.4: The performance of each extended AWF model.

Reynolds number	Original[%]	α function type [%]	Wall normal component [%]	Laminarization factor [%]
30,000	15.18	16.06	15.20	15.80
60,000	8.57	9.29	8.52	8.95
90,000	9.06	9.34	8.88	9.53
AVERAGE	10.94	11.56	10.87	11.43

Table4.5: The performance of the AWF with different mesh.

Reynolds number	Mesh 1[%]	Mesh2[%]	Mesh3[%]
30,000	15.18	12.56	9.17
60,000	8.57	8.29	8.40
90,000	9.06	8.43	10.21
AVERAGE	10.94	9.76	9.26

CHAPTER 5: Conclusions

I: The WF models can save more than 90% mesh used for the LRN model.

II: The AWF predicted slightly closer results to the LRN's results than the conventional WF model in velocity and turbulence field.

III: The AWF improved thermal field prediction by 31.2% than the conventional WF model.

IV: The extended forms of the AWF showed slight improvement in the bend region and after the turn region. But, for the whole region, they did not show improvement. (The total error from the experimental results was worse than the original result.)

V: The extended AWF may need re-tuning model parameters for three dimensional calculations.

VI: Using finer mesh, the AWF showed predict better results.

VII: From the conclusion stated above, the AWF has much potential to be more reliable wall function for three dimensional calculations. However, further study will be necessary to ensure better results in three dimensional and complex flows.

REFERENCES

[1]: Launder, B., Sharma, B., 1974 “Application of the energy dissipation model of turbulence the calculation of flow near a spinning disc.,” Lett.Heat Mass Transfer, 1, pp.131-138.

[2]: Launder, B., Spalding, D., 1974, “The numerical computation of turbulent flows,” Comput. Methods in Appl. Mech. Eng., 3 (2),pp. 269-289.

[3]: Thomas, L.C., Hasris, S.M.F., 1989, “Supplementary boundary-layer approximations for turbulent flow,” J.of Fluid Eng. 111, pp420-427.

[4]: Chieng, C.C., Launder, B.E., 1980, “On the calculation of turbulent heat transport downstream from an abrupt pipe expansion,” Numer. Heat Transfer, 3, pp.189–207.

[5]: Amano, R.S., 1984, ”Development of turbulence near wall model and its application to separated and reattached flows,” Numer. Heat Transfer, 7, pp.59-76.

[6]: Ciofallo, M., Collins, W.M., 1989, “k-e predictions of heat transfer in turbulent re-circulating flows using an improved wall treatment,” Numer. Heat Transfer, 15, pp. 21 -47.

[7]: Barenblatt, G.I., Chorin, A.J., Prostokishin, V.M., 2002. “A model of a turbulent boundary layer with a nonzero pressure gradient,” Proc. Natl. Acad. Sci., 99, pp.5772-5776.

[8]: Kader, B.A., 1991, “Heat and mass transfer in pressure-gradient boundary layers,” Int. J. Heat Mass Transfer, 34, pp.2837-2857.

[9]: Craft, T.J., Gant, S.E., Gerasimov, A.V., Iacovides, H., Launder, B.E., 2006, “Development and application of wall-function treatments for turbulent forced and mixed convection flows,” Fluid Dyn. Res., 38, pp.127-144.

[10]: Knopp, T., Alrutz, T., Schwamborn, D., 2006, “A grid and flow adaptive wall-function method for RANS turbulence modeling,” J. Comput. Phys., 220, pp.19-40.

[11]: Popovac, M., Hanjalic´, K., 2007, “Compound wall treatment for RANS computation of complex turbulent flows and heat transfer,” Flow Turbul. Combust., 78, pp.177-202.

[12]: Utyuzhnikov, S.V., 2008, “Robin-type wall functions and their numerical implementation,” Appl. Numer. Math., 58, pp.1521-1533.

[13]: Craft, T.J., Gerasimov, A.V., Iacovides, H., Launder, B.E., 2002, “Progress in the generalization of wall-function treatments,” Int. J. Heat Fluid Flow 23, 148-160.

[14]: Mostafa, N., 2007, “Computational studies of blade cooling related turbulent flows,” Ph.D. Thesis, University of Manchester, Manchester, UK.

[15]: Gerasimov, A.V., 2003, “Development and application of an analytical wall-function strategy for modelling forced, mixed and natural convection flows. Ph.D. Thesis, University of Manchester, Manchester, UK.

[16]: Ishibashi, Y, 2012, “An Analytical Wall-Function for Turbulent Heat Transfer in Separating-Reattaching and Impinging Flows,” Master Thesis, Osaka Prefecture University, Sakai, Japan

[17]: Suga, K., 2007, “Computation of high Prandtl number turbulent thermal fields by the analytical wall-function,” Int. J. Heat Mass Transfer, 50, pp.4967-4974.

[18]: Suga, K., Nishiguchi, S., 2009, “Computation of turbulent flows over porous/fluid interfaces,” Fluid Dyn. Res. 41, pp.12401-12416.

[19]: Suga, K., Kubo, M., 2010, “Modeling turbulent high Schmidt number mass transfer across undeformable gas-liquid interfaces,” Int. J. Heat Mass Transfer, 53, pp.2989-2995.

[20]: McDonald, C.F., 2012,"Helium turbine machinery operating experience from gas turbine power plants and test facilities," App. Therm. Eng. 44 pp.108-142

[21]: Xie, G., Sundén, B., 2010, "Numerical predictions of augmented heat transfer of an internal blade tip-wall by hemispherical dimples," Int. J. Heat Mass Transfer, 53, pp.5639-5650

[22]: Sundén, B. and Faghri,M., 2001, "Heat Transfer in Gas Turbines," WIT Press, Southampton, UK.

[23]: Goldstein, R.J., 2001, "Heat Transfer in Gas Turbine Systems," Ann NY Acad Sci, New York, NY.

[24]: Han, J.C., Dutta,S., and Ekkad, S.V., 2000, "Gas Turbine Heat Transfer and Cooling Technology," Taylor & Francis, New York, NY.

[25]: Iacovides, H., Kounadis, D., Xu, Z., 2009, "Experimental study of thermal development in a rotating square-ended U-bend," Exp. Therm Fluid Sci., 33, pp.482-494.

[26]: Su, G., Chen, H.C., Han, J.C., Heidmann, J.D., 2004, "Computation of flow and heat transfer in rotating two-pass rectangular channels (AR=1:1, 1:2 and 1:4) with smooth walls by a Reynolds stress turbulence model", Int. J. Heat Mass Transfer, 47, pp.5665-5683.

[27]: Iacovides, H., Nikas, K.S.P., 2002, "The computation of flow and heat transfer through an orthogonally rotating square-ended U-bend, using low-Reynolds-number models," Eng. Turbul. Model. Exp., 5, pp.811-820.

[28]: Sthephanie, B., 2001, "A Beginner's Guide to Uncertainty of Measurement, " Center for Basic, Thermal and Length Methodology, NPL, UK

[29]: Lien, F., Leschziner, M., 1994, "A general non orthogonal finite volume algorithm for turbulent flow at all speeds incorporating second-moment turbulence transport closure," Comput. Methods Appl. Mech. Eng., 114, pp.123–167.

[30]: Leschziner, M.A., Lien, F.S., 1994, "Upstream monotonic interpolation for scalar transport with application to complex turbulent flows," Int. J. Numer. Methods Fluids, 19, pp.527‑548.

[31]: Patanker, S., 1980, "Numerical heat transfer and fluid flow," Taylor & Francis, New York, NY, the U.S, pp. 113-126.

[32]: Rhie, C., Chow, W., 1983, "Numerical study of the turbulent flow past an airfoil with trailing," AIAA J., 21, pp.1525-1532.

[33]: Patanker, S., 1980, "Numerical heat transfer and fluid flow," Taylor & Francis, New York, NY, the U.S. pp.64-66.

[34]: Craft, T.J., Graham, L.J.W., Launder, B.E., 1993,"Impinging jet studies for turbulence model assessment. Part 2: An examination of the performance of four turbulence models," Int. J. Heat Mass Transfer 6, pp.2685–2697.